Available online at www.sciencedirect.com
SCIENCE DIRECT®
Geochimica et Cosmochimica Acta 70 (2006) 2622–2642
Geochimica
www.elsevier.com/locate/gca

Crystallization of melilite from CMAS-liquids and the formation of the melilite mantle of Type B1 CAIs: Experimental simulations

Ruslan A. Mendybaev [a,b,*], Frank M. Richter [a,b], Andrew M. Davis [a,b,c]

[a] Department of the Geophysical Sciences, The University of Chicago, Chicago, IL 60637, USA
[b] Chicago Center for Cosmochemistry, The University of Chicago, Chicago, IL 60637, USA
[c] Enrico Fermi Institute, The University of Chicago, Chicago, IL 60637, USA

Received 10 August 2005; accepted in revised form 17 February 2006

Abstract

Type B CAIs are subdivided into B1s, with well-developed melilite mantles, and B2s, with randomly distributed melilite. Despite intensive study, the origin of the characteristic melilite mantle of the B1s remains unclear. Recently, we proposed that formation of the melilite mantle is caused by depletion of the droplet surface in volatile magnesium and silicon due to higher evaporation rates of volatile species compared to their slow diffusion rates in the melt, thus making possible crystallization of melilite at the edge of the CAI first, followed by its crystallization in the central parts at lower temperatures. Here, we present the results of an experimental study that aimed to reproduce the texture observed in natural Type B CAIs. First, we experimentally determined crystallization temperatures of melilite for three melt compositions, which, combined with literature data, allowed us to find a simple relationship between the melt composition, crystallization temperature, and composition of first crystallizing melilite. Second, we conducted a series of evaporation and cooling experiments exposing CAI-like melts to gas mixtures with different oxygen fugacities (f_{O_2}). Cooling of the molten droplets in gases with $\log f_{O_2} \geqslant$ IW-4 resulted in crystallization of randomly distributed melilite, while under more reducing conditions, melilite mantles have been formed. Chemical profiles through samples quenched right before melilite started to crystallize showed no chemical gradients in samples exposed to relatively oxidizing gases ($\log f_{O_2} \geqslant$ IW-4), while the near-surface parts of the samples exposed to very reducing gases ($\log f_{O_2} \leqslant$ IW-7) were depleted in volatile MgO and SiO_2, and enriched in refractory Al_2O_3. Using these experimental results and the fact that the evaporation rate of magnesium and silicon from CAI-like melts is proportional to $\sqrt{P_{H_2}}$, we estimate that Type B1 CAIs could be formed by evaporation of a partially molten precursor in a gas of solar composition with $P_{H_2} \geqslant 10^{-4}$ bar. Type B2 CAIs could form by slower evaporation of the same precursors in the same gas with $P_{H_2} \leqslant 10^{-5}$ bar.

1. Introduction

Refractory coarse-grained calcium-, aluminum-rich inclusions (CAIs) in carbonaceous chondrites are the oldest known materials to have formed in the Solar System (Allègre et al., 1995; Lugmair and Shukolyukov, 2001; Amelin et al., 2002) and as such they contain chemical and isotopic evidence of processes that operated during the early stages of the evolution of the Solar System. CAIs in CV chondrites are typically about 1 cm in diameter and classified into Type A, composed of melilite and spinel with minor amounts of perovskite and hibonite, and Type B, consisting mainly of melilite, spinel, and fassaite with relatively small amounts of anorthite (e.g., Grossman, 1975; MacPherson et al., 1988; MacPherson, 2003). The mineralogy and mineral chemistry of CAIs and that predicted by thermodynamic calculations of a cooling gas of solar composition led Grossman (1972) to suggest that CAIs represent high-temperature condensates from the cooling solar nebula. There is also textural evidence that after the Type B CAIs condensed, they were reheated and partially melted to a high degree such that the only mineral remaining was spinel. One would expect that some fraction of the more volatile elements in CAIs (i.e., silicon and magnesium) would have evaporated during this high-temperature

* Corresponding author. Fax: +1 773 702 9505.
E-mail address: ramendyb@uchicago.edu (R.A. Mendybaev).

0016-7037/$ - see front matter © 2006 Elsevier Inc. All rights reserved.
doi:10.1016/j.gca.2006.02.018

stage, which could explain their depletion in MgO and SiO_2 compared to the calculated compositions of partial condensates from a cooling solar gas (Grossman et al., 2000). CAIs are also often enriched in the heavy isotopes of magnesium and silicon (Wasserburg et al., 1977; Clayton et al., 1978; Molini-Velsko et al., 1986), which is generally taken as strong evidence of partial evaporation of these elements. The following scenario for formation of Type B CAIs has been proposed (Grossman et al., 2000) based on textural, mineralogical, chemical, and isotopic data. (1) The precursor materials of the Type B CAIs condensed from a hot gas of solar composition as it cooled to temperatures in the range 1050–1170 °C (for P_{H_2} in the range 10^{-3}–10^{-5} bar). (2) These precursor materials were rapidly reheated to about 1400 °C and then cooled at rates of 1–50 °C h^{-1} to produce coarse-grained igneous textures (Stolper and Paque, 1986). During this reheating and subsequent cooling, a significant fraction of the original magnesium and silicon was lost by evaporation, producing the observed heavy isotope enrichments of these elements.

The Type B CAIs are subdivided texturally into Types B1 and B2 (Wark and Lovering, 1982). Type B1 CAIs are concentrically zoned with a continuous outer layer of melilite (the mantle) enclosing an interior part with a relatively random distribution of melilite, fassaite, and anorthite. The Type B2 CAIs do not have a melilite mantle and the entire inclusion is much like the interior parts of the B1s. Spinel is distributed throughout both Type B1 and B2 CAIs. The bulk compositions of B1s and B2s are similar, although Simon and Grossman (2003) have suggested that some B2s are more pyroxene-rich than typical B1s. Despite intensive study, the origin of the characteristic melilite mantle of the B1s remains unclear. Wark and Lovering (1982) suggested that the melilite mantle of the B1s was formed by relatively fast inward fractional crystallization of completely molten droplets. However, why crystallization started at the surface, and why this would result in a melilite mantle in the case of the Type B1 inclusions but not in B2s was not explained. It has also been proposed that the melilite mantles formed by crystallization of new molten material that was added at a late stage onto a previously formed core or by accretion of melilite directly from a surrounding gas onto the preexisting core (Meeker, 1995). In our view, any explanation for the origin of the melilite mantle of the Type B1 CAIs will be incomplete if it does not also explain why the Type B2 CAIs, which are very similar in size and bulk composition to the B1s, have no melilite mantle. Recently, we suggested that the formation of melilite mantles in the Type B1s and their absence in B2s might be due to differences in the evaporation rates of magnesium and silicon from the surface of the partially molten droplets relative to their diffusion rates in the melt (Richter et al., 2002b, 2006). If the evaporation rates are slow compared to diffusion, the system would remain chemically homogeneous, and it is reasonable to expect a relatively uniform distribution of minerals to develop as the system cools. The resulting texture would be similar to that of the B2s. On the other hand, if the evaporation rates of magnesium and silicon are sufficiently fast compared to diffusion rates in the melt, the outer parts of the molten droplets would become depleted in magnesium and silicon, causing relatively gehlenitic melilite to crystallize first in the outer parts of the cooling droplet followed later by the crystallization of more åkermanitic melilite in the central parts of the droplet. The early preferential crystallization of melilite in the more silicon- and magnesium-depleted melt at the surface would give rise to a melilite mantle similar to that characteristic of the Type B1 CAIs.

The coarse-grained igneous texture of B2s has been reproduced experimentally by cooling partially molten droplets (spinel + melt) of a Type B-like composition (Paque and Stolper, 1984; Stolper and Paque, 1986). To the best of our knowledge, zoned textures similar to those of B1s have not been reproduced experimentally apart from our report in Richter et al. (2006). Here, we use laboratory experiments to explore the viability of our suggestion that B1 textures will arise when the evaporation of silicon and magnesium from the surface of a molten droplet is too fast for diffusion to maintain chemical homogeneity. We also present new experimental results on the crystallization sequence of minerals during cooling of molten CAI-like compositions. By combining our results with those from several earlier crystallization experiments we find a simple systematic relationship for the crystallization temperature of melilite as a function of melt composition. This relationship shows that melilite will crystallize first in those regions depleted in silicon and magnesium, which is a necessary condition for our suggestion for how melilite mantles form as a molten system cools. Having established the plausibility of our proposition for the origin of melilite mantles, we undertook a more direct approach of actually crystallizing melilite under different conditions in order to produce B1 or B2 textures. The conceptual model and preliminary experimental results of the work presented here were published as extended abstracts by Richter et al. (2002b), Mendybaev et al. (2003a,b), and Davis et al. (2003) and were outlined in a short paper (Richter et al., 2006). Here, we present the detailed experimental data in support of the model.

2. Experimental techniques

We conducted three types of experiments. (1) The crystallization temperatures of melilite from melts of various compositions were determined using the approach of Stolper (1982) and Beckett (1986). These equilibrium crystallization experiments were used to establish the temperature and composition dependences of melilite crystallization. (2) Partially molten droplets were cooled at different rates under relatively oxidizing conditions (in air or in gas mixtures with oxygen fugacities corresponding to the iron–wüstite buffer), such that the loss of magnesium and silicon by evaporation was negligible. Except for our using different starting melt compositions, these isochemical crystalli-

zation experiments were analogous to those done by Paque and Stolper (1984) and Stolper and Paque (1986) to explore the effect of cooling rate on mineral texture. (3) Molten droplets were exposed to a flowing gas with extremely low f_{O_2}, either at a fixed temperature or while cooling at a controlled rate. Under very reducing conditions the molten samples lose significant amounts of silicon and magnesium via the evaporation reactions

$$MgO_{(l)} \rightarrow Mg_{(g)} + \tfrac{1}{2}O_{2(g)} \quad (1)$$

and

$$SiO_{2(l)} \rightarrow SiO_{(g)} + \tfrac{1}{2}O_{2(g)} \quad (2)$$

The evaporation rate of an element i is described by the Hertz–Knudsen equation:

$$J_i = \frac{n\gamma_i(P_{i,\mathrm{sat}} - P_i)}{\sqrt{2\pi m_i RT}}, \quad (3)$$

where J_i is the flux of i in moles per unit per unit time, n is the number of atoms of i in the dominant gas phase species molecule containing i, γ_i is the evaporation coefficient, $P_{i,\mathrm{sat}}$ is the saturation vapor pressure of the dominant gas species containing i, P_i is the pressure of i at the evaporating surface, m_i is the molecular weight of the gas species containing i, R is the gas constant, and T is the absolute temperature (e.g., Richter et al., 2002a). In free evaporation (i.e., vacuum furnace experiments with $P_i \ll P_{i,\mathrm{sat}}$), the evaporation rates increase as $\sqrt{f_{O_2}}$ because $P_{i,\mathrm{sat}} \propto \sqrt{f_{O_2}}$ (see Richter et al., 2002a). Our evaporation experiments, which are run in a 1-bar gas-mixing vertical tube furnace, are not run under true free evaporation conditions but are rather in the limit $P_i \rightarrow P_{i,\mathrm{sat}}$. Such experiments will produce elemental fractionations of the residues that are similar to those by free evaporation as long as the very nearly saturated gas is continuously removed. This is because the net flux of each volatile species is proportional to the product of the saturation vapor pressure times the gas flow rate. The various volatile species lost from the system over time were derived from the net evaporation of the molten droplet in our experiments. We can control the net evaporation rates of silicon and magnesium by appropriately adjusting the f_{O_2} and flow rate of the surrounding gas. In oxidizing to moderately reducing conditions ($\log f_{O_2} > \mathrm{IW\text{-}4}$), the saturation vapor pressures are sufficiently small that evaporation is negligible over the duration of our experiments. Measurable loss of MgO and SiO_2 occurs in experiments with $\log f_{O_2} < \mathrm{IW\text{-}4}$. Under extremely reducing conditions ($\log f_{O_2} < \mathrm{IW\text{-}6}$), the evaporation rates become sufficiently fast compared to diffusion that significant chemical gradients can arise in the residue.

2.1. Starting materials

Three compositions were used as starting materials (Table 1): (1) CAIB-R, a composition close to average Type B CAIs; (2) DT1, similar in composition to composition δ of Grossman et al. (2002), which falls on the condensation curve of a cooling gas of solar composition at 10^{-3} bar total pressure; and (3) DT2, which lies along the evaporation trajectory of DT1. The starting materials were prepared by mixing appropriate amounts of MgO (Alfa Aesar®, 99.998%), SiO_2 (Aldrich®, >99.995%), Al_2O_3 (Alfa Aesar®, 99.99%), and $CaCO_3$ (Alfa Aesar®, 99.99%) and then grinding the mixture under ethanol in an agate mortar for at least 1 h. Several batches of about 1 g each were prepared for all three compositions. After the mixtures were dried at room temperature, they were placed in individual platinum crucibles and slowly heated in a muffle furnace to 1000 °C over about 10 h and held at this temperature for 5–10 h in order to drive off CO_2. The platinum crucibles were removed from the muffle furnace, cooled in air, placed in a high-temperature furnace at 1560–1665 °C (depending on starting composition and purpose of experiment) for up to 15 h, and finally quenched in air. The quench products (clear glass or glass with a small amount of spinel) were removed from the crucible and ground under ethanol in an agate mortar for about 1 h. The resulting powders were mixed with polyvinyl alcohol, loaded onto platinum or iridium wire loops 2.5–6.0 mm in diameter, and then allowed to dry for at least 12 h before being used in crystallization or evaporation experiments. In order to avoid evaporation and recrystallization of the wire loops, platinum was used in experiments conducted in conditions more oxidizing than iron–wüstite and iridium for more reducing conditions.

Table 1
Chemical composition (in wt%) of the starting materials used in the experiments

	CaO	MgO	Al_2O	SiO_2
CAIB-R	30.4	9.6	28.6	31.4
DT1	25.7	13.5	30.2	30.6
DT2	27.0	11.7	33.0	28.3

All crystallization experiments are effectively closed systems, in that they were run in air and evaporation is negligible for all the major components of the melt. The evaporation experiments were carried out using nominally pure H_2 or H_2–CO_2 gas mixtures (99.99% H_2, 99.8% CO_2) with N_2 (99.998%) used as a purge gas.

2.2. Experimental protocol

The experiments were conducted in a Deltech 1 atm vertical tube furnace equipped for gas mixing. The furnace configuration was identical to that used for the silicon carbide evaporation experiments of Mendybaev et al. (2002). The temperature in the furnace hot spot was measured by a Type S (Pt-$Pt_{90}Rh_{10}$) thermocouple located inside an yttria-doped zirconia oxygen sensor ($SIRO_2$®, Ceramic Oxide Fabricators, Ltd., Eaglehawk, Australia) that was placed adjacent to the sample. The thermocouple was calibrated at the melting point of gold (1064.4 °C) and reported temperatures are believed accurate to ±3 °C. Temperature was controlled with a Eurotherm 812 control-

ler/programmer and cooling rates were varied from 0 to 400 °C h^{-1}. Gases were introduced into the furnace from the top of the 3.2 cm diameter alumina tube (99.8% Al_2O_3; Vesuvius McDanel, Malvern, PA) and exhausted from the bottom. The gas flow rates were measured by FM-1050 flowmeter with E300 tube (Matheson, Montgomeryville, PA). The oxygen fugacity of the flowing gas was measured using a $SIRO_2^{®}$ oxygen sensor corrected for non-Nernstian behavior of the electrolyte (Mendybaev et al., 1998). Uncertainties in log f_{O_2} were better than ±0.05 in conditions near the iron–wüstite (IW) buffer, ~±0.2 at IW-6, and ~±0.5 at IW-9. Due to the high temperatures of our experiments no catalysts were required to equilibrate the gas mixtures (Beckett and Mendybaev, 1997).

In experiments designed to determine the crystallization temperature of melilite, a sample was brought directly into the furnace hot spot by lowering an alumina tube holding a platinum wire loop containing the sample. The sample was held at constant temperature for a predetermined period of time and then quenched in air or in deionized water. The crystallization experiments were conducted in flowing air or a H_2–CO_2 mixture with $\log f_{O_2} > IW$. Oxidizing conditions were chosen in order to avoid any significant evaporation of silicon and magnesium.

A sample used in the isochemical cooling experiments was first melted at a desired temperature for at least 3 h as described above. The sample was then quickly removed from the furnace, weighed, placed back in the hot spot of the furnace, and then cooled at controlled rate. Once the temperature had dropped to a predetermined value, the sample was quenched in deionized water or in air.

Samples used in the evaporation experiments under extremely reducing conditions were first melted for at least 3 h under sufficiently oxidizing conditions that evaporation would be negligible. The sample was then removed from the furnace, weighed, and returned into the cold zone of the furnace. The oxidizing gas was then replaced by nominally pure hydrogen or H_2–CO_2 gas mixtures with $\log f_{O_2} < IW-4$. Once the e.m.f. reading of the oxygen sensor had stabilized at a value indicating that the desired f_{O_2} had been reached (30–45 min), the sample was lowered into the hot spot of the furnace to begin an evaporation experiment. The experiment was ended by pulling the sample up to the cold part of the furnace, turning off the flow of the reducing gas, and flushing the furnace with N_2. The sample was then removed and weighed again to determine the extent of evaporation. All weight loss was attributed to sample evaporation, because no measurable weight loss from iridium wires occurred in several "blank" experiments.

Thick sections of the starting materials and run products were prepared by cutting the samples with a diamond blade, mounting them in epoxy, and then polishing the mount with diamond pastes. The sections were examined using a JEOL JSM-5800LV scanning electron microscope (SEM) with an Oxford/Link ISIS-300 X-ray microanalysis system. The composition of the starting materials was determined by analyzing clear glass that had been produced by melting the starting powder. All starting glasses were found to be homogeneous and the composition was obtained by averaging 20–200 spot analyses. The composition of melilite and other phases in the run products was obtained from spot analyses of the mineral cores or along traverses crossing the central parts of the grains. In some cases detailed Åk maps of melilite were made from quantitative maps, in which a quantitative analysis was made of each spot in a grid of 64×48, 128×96 or 256×192 spots. The relative proportions of the various phases present in the run products were obtained by image analysis of backscattered electron images and X-ray maps.

3. Experimental results and discussion

3.1. Crystallization of melilite under oxidizing conditions

3.1.1. CAIB

In order to check our experimental procedures, we first determined the crystallization temperature of melilite for a melt composition (CAIB-R) that had already been studied in detail by Stolper (1982). The experimental conditions and results are presented in Table 2 and Fig. 1a.

Magnesium–aluminum spinel is known to be the first phase to crystallize from a melt of CAIB-R composition ($T \sim 1550$ °C as reported by Stolper, 1982). In all of our experimental charges, spinel appeared as very small (2–20 μm) euhedral grains comprising ~10–15 vol% of the samples (Table 2), which is consistent with the results reported by Stolper (1982). The distribution of spinel within the samples was quite variable, sometimes relatively homogeneous but often with the spinel grains being concentrating in the bottom and/or top portions of the quenched run products.

In our experiments, melilite starts to crystallize at about 1410 ± 10 °C, in good agreement with the crystallization temperature of $T \sim 1400$ °C reported by Stolper (1982). In the isothermal crystallization experiments, melilite occurs as small (10–40 μm) relatively homogeneously distributed grains (Fig. 2a). The first melilite to crystallize from a CAIB-R melt is relatively aluminum-rich and magnesium-poor. Melilite is a solid solution between gehlenite ($Ca_2Al_2SiO_7$) and åkermanite ($Ca_2MgSi_2O_7$) and the early-crystallized melilite has 19 ± 3 mol% åkermanite ($Åk_{19\pm3}$), but becomes more abundant and more åkermanitic (up to ~34 vol% and $Åk_{36\pm9}$ at 1245 °C) as the temperature decreases (see Table 2). Detailed X-ray maps showed that despite their small size, the melilite grains from the isothermal experiments are usually normally zoned with their central part being slightly depleted in magnesium and silicon (i.e., low Åk) and enriched in aluminum compared to the more åkermanitic outer parts. Such normal zoning is expected because, as the first relatively gehlenite-rich melilite starts to crystallize, the residual melt becomes enriched in magnesium and depleted in aluminum, such that later crystallizing melilite must become more åkermanitic. The range of Åk content

Table 2
Conditions and results for CAIB crystallization experiments

Run	T (°C)	Duration (h)	Phases identified	Melilite		Notes[b]
				Comp[a]	Vol%	
CAIB-R2	1436	19.0	gl + sp			
CAIB-R16	1418	26.9	gl + sp			Three hours at 1433 °C then cooled at 10 °C h^{-1} to 1418 °C and held for 26.9 h
CAIB-R15	1411	45.8	gl + sp			
CAIB-R4	1410	16.8	gl + sp + mel	$Åk_{19\pm3}$	5	
CAIB-R14	1400	23.0	gl + sp[c]			Three hours at 1435 °C then cooled at 10 °C h^{-1} to 1400 °C and held for 23.0 h
CAIB-R18	1394	43.0	gl + sp + mel	$Åk_{21\pm3}$	3	Three hours at 1433 °C then cooled at 10 °C h^{-1} to 1394 °C and held for 43.0 h
CAIB-R17	1360	47.8	gl + sp + mel	$Åk_{23\pm3}$	10	
CAIB-R11	1351	27.6	gl + sp + mel	$Åk_{25\pm2}$	16	
CAIB-R7	1336	23.8	gl + sp + mel	$Åk_{27\pm2}$	13	
CAIB-R1[d]	1310	18.8	gl + sp + mel	$Åk_{28\pm2}$	21	
CAIB-R3[d]	1309	20.9	gl + sp + mel	$Åk_{29\pm1}$	20	Three hours at 1000 °C then heated at 400 °C h^{-1} to 1309 °C and held for 20.9 h
CAIB-R6	1306	28.6	gl + sp + mel	$Åk_{27\pm4}$; $Åk_{36\pm4}$[e] Avg: $Åk_{32\pm8}$	35	Five hours at 1430 °C then cooled at 10 °C h^{-1} to 1306 °C and held for 28.6 h
CAIB-R10	1299	27.9	gl + sp + mel	$Åk_{33\pm3}$	15	
CAIB-R8	1275	42.0	gl + sp + mel	$Åk_{35\pm5}$	23	
CAIB-R9	1245	41.7	gl + sp + mel	$Åk_{36\pm9}$	34	Quenched in air
CAIB-R12	1226	138.0	sp + mel + an	$Åk_{27–80\ (31\pm4)}$[f]	28	Quenched in air
CAIB-R13	1195	160.6	sp + mel + an	$Åk_{24\text{-}86\ (31\pm3)}$[f]	24	

[a] Shown are average melilite compositions with 1σ standard deviation obtained from analysis of central parts of at least 40 individual grains about 10–20 μm in size. Melilite was found as one large euhedral crystal in CAIB-R18 and three crystals in CAIB-R6, and composition of melilite represents average composition obtained from detailed X-ray map.

[b] Experiments were conducted by bringing the samples directly into the furnace hot spot with temperature of interest unless noted.

[c] The lack of melilite in a polished section of CAIB-R14 quenched at 1400 °C might be due to the section not intersecting any of a small number of melilite crystals actually present.

[d] Note that CAIB-R1 and CAIB-R3 have same texture and melilite compositions despite their different thermal histories suggesting that melilite either did not have enough time to crystallize and grow while temperature was increasing from 1000 to 1309 °C or low temperature melilite seeds were re-equilibrated with the melt at the higher temperatures.

[e] Bimodal distribution of melilite compositions.

[f] Wide range of melilite compositions with a distinct peak shown in parentheses.

in melilite from CAIB-R4 crystallized at 1410 °C varies from $Åk_{16}$ to $Åk_{27}$, while melilite from CAIB-R9 crystallized at 1245 °C is characterized by a significantly wider range of compositions: from $Åk_{22}$, presumably the earliest melilite crystallized at about 1400 °C, to $Åk_{57}$ for the last melilite to crystallize.

Melilite grains from the experiments conducted at subsolidus temperatures ($T < 1230$ °C, as determined by Stolper, 1982; for composition CAIB) are 5–20 μm in size and very irregular in shape (Fig. 2b). The melilite composition is extremely heterogeneous, varying from $Åk_{24}$ to $Åk_{86}$ at 1195 °C (Table 2), with a distinct peak around $Åk_{31}$ (width at half height of the Gaussian distribution corresponds to $\pm Åk_4$). The very wide range of melilite composition suggests that chemical equilibrium has not been reached in these experiments even after 5 days. The time scale required for homogenization of 20 μm melilite grains at 1200 °C is estimated to be several weeks based on cation diffusion in melilite (Richter et al., 2006).

Heating samples to temperatures above the crystallization temperature of melilite (1410 °C for composition CAIB-R), followed by slow cooling, results in the formation of very large euhedral melilite grains such as the one shown in Figs. 2c and 3. Similar textures were observed by Stolper and Paque (1986) when they slowly cooled partially molten CAIB droplets in air at rates <50 °C h^{-1}. These large euhedral melilite grains are usually normally zoned but sometimes they show complex zoning patterns, including sector zoning as discussed below. Fig. 3 is an åkermanite map of the sample CAIB-R6, cooled from 1430 to 1306 °C at 10 °C h^{-1} and held at this temperature for an additional 29 h before quenching. The map was constructed from quantitative maps consisting of 49,152 spot analyses for MgO, Al_2O_3, SiO_2, and CaO. Fig. 3 shows that these large euhedral melilite grains are normally zoned with compositions typically varying from $\sim Åk_{25–30}$ in the central parts of the grains to $\sim Åk_{45}$ in the outer parts. The fact that that melilite remains zoned even after 29 h of heating at 1306 °C suggests low cation diffusion rates in melilite, which will be discussed later. In some parts of the outer edge of the grains the melilite becomes more gehlenitic again, which we believe is associated with melilite that crystallized during quenching.

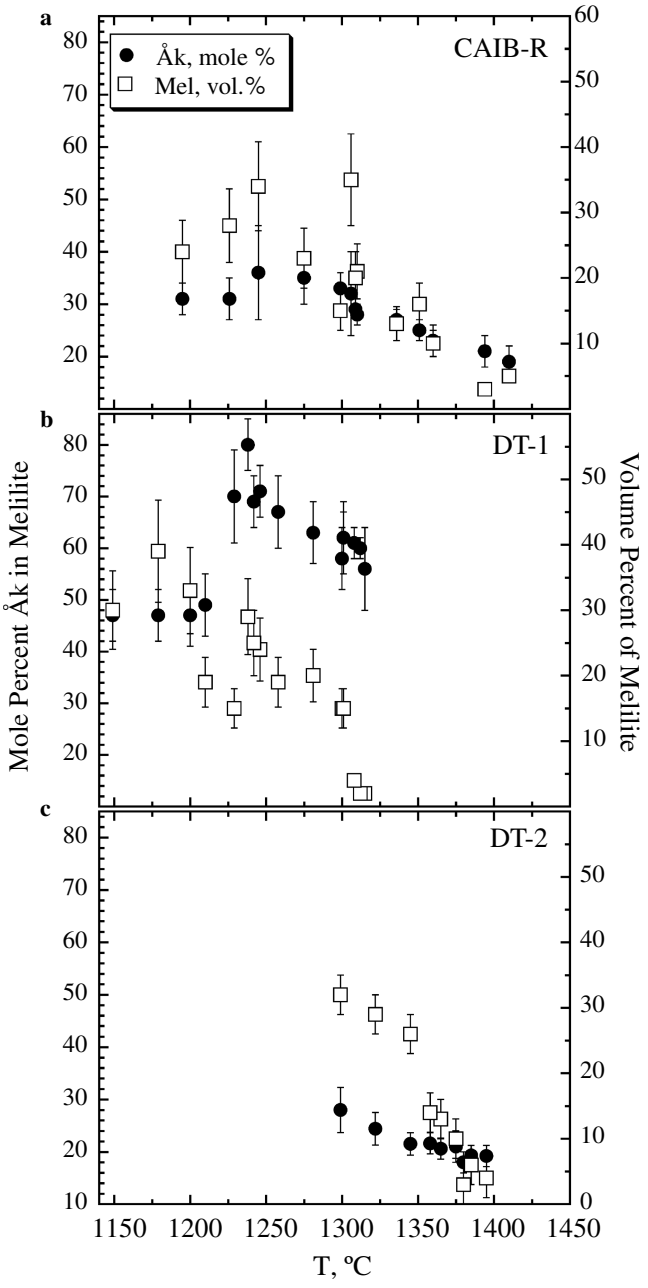

Fig. 1. Measured abundances of melilite (vol%) and composition of melilite grain cores (presumably the first melilite to crystallize) in experimental run products as a function of crystallization temperature from: (a) CAIB-R melt, (b) DT1 melt, and (c) DT2 melt.

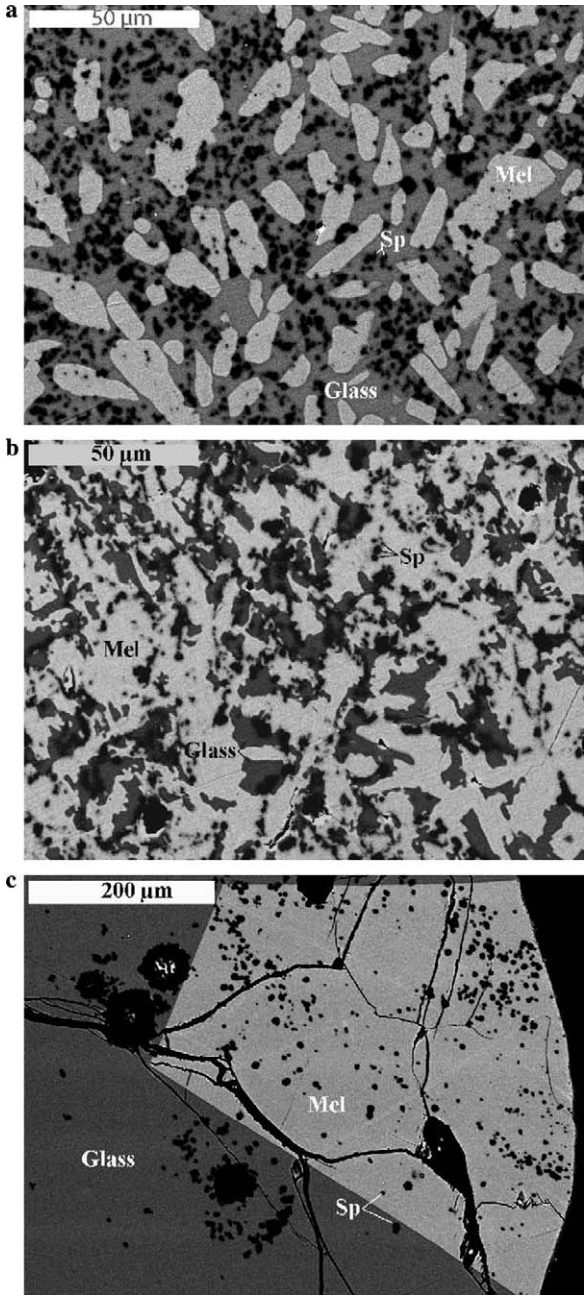

Fig. 2. Typical textures observed in run products crystallized from CAIB-R composition at: (a) subliquidus temperatures (sample CAIB-R11, 1351 °C); (b) subsolidus temperatures (sample CAIB-R13, 1195 °C); and (c) sample CAIB-R18 which was heated for 3 h at 1433 °C, cooled to 1394 °C at 10 °C h^{-1} in air, and then held at this temperature for 43 h, forming a large euhedral melilite grain (~500 µm).

3.1.2. DT1

The composition of the starting material DT1 is close to the composition labeled δ on the condensation curve of Grossman et al. (2002). The conditions and results of the crystallization experiments are given in Table 3. The relative abundance of melilite and the average composition of the central parts of the melilite grains formed in these experiments are shown in Fig. 1b.

Stoichiometric spinel ($MgAl_2O_4$) with a typical grain size of about 10 µm is the first mineral to crystallize from a DT1 melt at $T > 1594$ °C, which is significantly higher than the 1550 °C reported by Stolper (1982) for spinel to crystallize in a CAIB composition. Table 3 shows that as the temperature decreases, the amount of spinel in the experimental charges first increases from 5 vol% at 1577 °C to 14 vol% at 1477 °C and then remains essentially constant at the lower temperatures. Stolper (1982) found a similar behavior for the proportion of spinel with decreasing temperature in his CAIB composition experiments. The

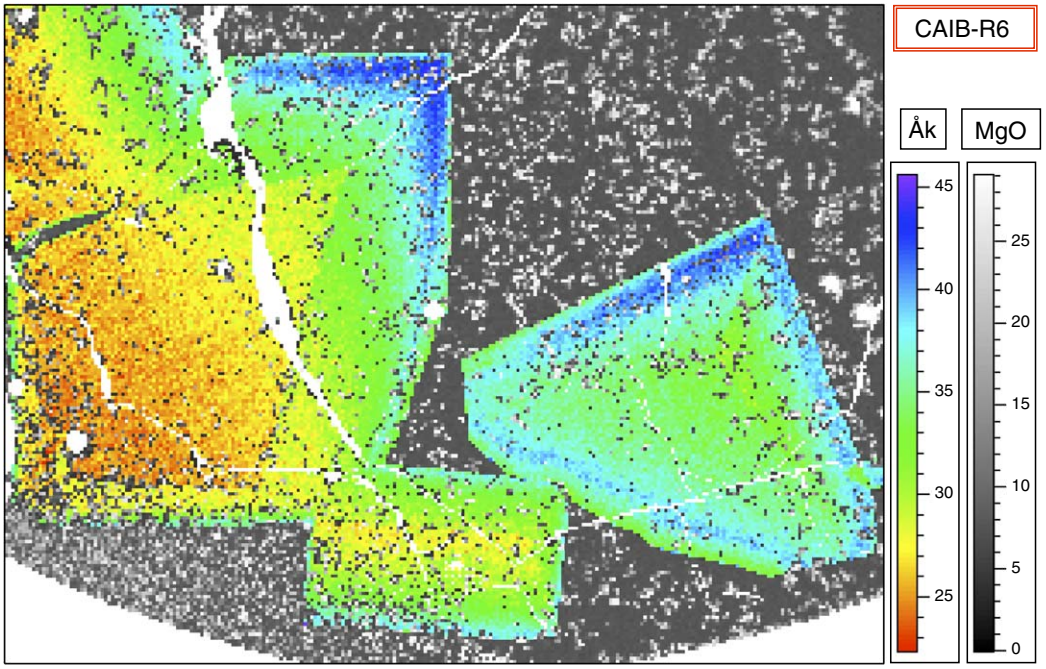

Fig. 3. Melilite compositional map of a portion of run CAIB-R6. This sample was heated for 5 h at 1430 °C, cooled to 1306 °C at 10 °C h^{-1}, and then held at this temperature for 29 h before quenching. The map shows normal zoning in melilite except at the extreme edges of crystals. The reverse zoning in outermost parts of the crystals most likely was formed during quenching. Field of view ~500 μm.

first melilite to crystallize from a DT1-composition melt was observed at 1315 °C, which is significantly lower than its crystallization temperature of 1410 °C from a melt with CAIB-R composition. This melilite is also much more åkermanitic ($Åk_{57\pm6}$) compared to first melilite crystallized from a CAIB-R melt (~$Åk_{19\pm3}$). Our experimentally determined crystallization temperature of melilite from the DT1 melt is considerably lower and its Åk content higher than calculated by Grossman et al. (2002). According to those calculations, melilite should begin to crystallize from a melt of δ composition (close to our DT1) at 1420 °C with a composition of $Åk_{24}$. The large difference between the calculated and experimentally measured crystallization temperature of melilite suggests that the thermodynamic model used by Grossman et al. (2002) for the melilite solid solution requires significant refinement and reaffirms the need for laboratory experiments to define the crystallization properties of Type B CAI-like melts.

Fig. 1b shows that, as was the case for CAIB-R, melilite becomes more abundant and more åkermanitic with decreasing temperature, reaching 30 vol% and $Åk_{>70}$ by 1230 °C. In experiments indicating subsolidus temperatures based on the texture of quenched run products ($T < 1225$ °C), melilite is typically $Åk_{47\pm5}$ (Fig. 1b), as in the case of DT1-1HH crystallized at 1179 °C and DT1-1EE crystallized at 1149 °C. The significantly lower Åk content of melilite in runs with $T < 1225$ °C is most likely due to equilibrium between melilite and melt not being reached in the subsolidus experiments.

The morphology of the melilite grains crystallizing from DT1 melt is very much like that of melilite crystallized from the CAIB-R composition. Melilite that has crystallized isothermally from DT1 melt at $T > 1238$ °C appears as small (typically ~10–20 μm) normally zoned grains very similar to those shown in Fig. 2a, while very irregular grains like those shown in Fig. 2b were observed in isothermal experiments at subsolidus temperatures. Large euhedral melilite grains were formed in experiments when droplets were partially melted at $T > 1315$ °C and then slowly cooled as was the case for experiments DT1-3A and DT1-3B. The texture observed in these experiments was very much like that shown in Fig. 2c. Melilite from experiments DT1-3A and DT1-3B has similar Åk content (from ~$Åk_{55}$ to ~$Åk_{70}$) and both samples show sector-zoned melilite, despite significantly different peak temperatures of 1351 and 1421 °C, respectively.

Sector zoning is caused by the growth of distinctive mineral compositions along different crystallographic axes. Such zoning has been observed in various natural and synthetic materials (e.g., Dowty, 1976; Beckett, 1986; Skulski et al., 1994; Steele et al., 1997) but to our knowledge it has not been previously reported for melilite. The sector-zoned melilite shown in Fig. 4a was produced in experiment DT1-3A, in which the sample was melted in air at 1351 °C for 5 h (the melilite crystallization temperature for the DT1 composition is 1315 °C as shown in Fig. 1b), cooled at 10 °C h^{-1}, and then quenched when temperature reached 1301 °C. A quantitative map of this melilite grain (Fig. 4a) shows a total compositional variation of $Åk_{55}$ to $Åk_{70}$, but with different chemical compositions along different crystallographic orientations. Fig. 4b shows two Åk profiles passing through the center of the crystal, one from the left edge of the grain to the right edge, and a second one from the top of the grain to the bottom. The pro-

Table 3
Conditions and results for DT1 crystallization experiments

Run	T (°C)	Duration (h)	Phases identified	Melilite comp[a]	Vol%			Notes[b]
					gl	sp	mel	
DT1-1PP	1646	1.2	gl					Quenched in air
DT1-1(c)	1594	11	gl + sp					Quenched in air
DT1-1F	1577	19.5	gl + sp		95	5		
DT1-1D	1560	13.6	gl + sp		93	7		
DT1-1A	1526	16.7	gl + sp		92	8		
DT1-1B	1477	14.7	gl + sp		86	14[c]		Five hours at 1526 °C then cooled to 1477 °C at 400 °C h^{-1}
DT1-1_Ir8	1473	16.5	gl + sp		86	14[c]		Five hours at 1526 °C then cooled to 1473 °C at 100 °C h^{-1}, IW, quenched in air
DT1-1_Pt3	1461	22.0	gl + sp		85	15[c]		Five hours at 1526 °C then cooled to 1461 °C at 65 °C h^{-1}, quenched in air
DT1-1P	1454	27.2	gl + sp		85	15		
DT1-1_Ir6	1447	42.0	gl + sp		86	14[c]		Three hours at 1526 °C then cooled to 1447 °C at 100 °C h^{-1}, IW, quenched in air
DT1-1_Pt4	1436	15.5	gl + sp		86	14[c]		Five hours at 1526 °C then cooled to 1436 °C at 90 °C h^{-1}, quenched in air
DT1-1O	1431	22.7	gl + sp					
DT1-1C	1428	23.4	gl + sp					Five hours at 1514 °C then cooled to 1428 °C at 70 °C h^{-1}
DT1-1E	1427	32	gl + sp					Five hours at 1526 °C then cooled to 1427 °C at 400 °C h^{-1}
DT1-1Y	1411	74.8	gl + sp		86	14		
DT1-1U	1401	40.3	gl + sp		84	16		
DT1-1N	1380	33.6	gl + sp					
DT1-1G	1379	21.7	gl + sp					Five hours at 1526 °C then cooled to 1379 °C at 400 °C h^{-1}
DT1-1W	1350	40.3	gl + sp		86	14		
DT1-1AA	1349	74.0	gl + sp		87	17		
DT1-1Z	1334	35.1	gl + sp		85	15		
DT1-1H	1333	39.3	gl + sp					Five hours at 1577 °C then cooled to 1333 °C at 245 °C h^{-1}
DT1-1GG	1329	33.1	gl + sp		86	14		Six hours 1349 °C then cooled to 1329 °C at 400 °C h^{-1}
DT1-1DD	1327	27.4	gl + sp		82	18		Quenched in air
DT1-1II	1322	32.4	gl + sp					Six hours 1349 °C then cooled to 1329 °C at 400 °C h^{-1}
DT1-1FF	1320	42.2	gl + sp		85	15		Quenched in air
DT1-1CC	1315	38.8	gl + sp + mel	$Åk_{57\pm4}$	81	17	2	
DT1-1LL	1312	17.1	gl + sp + mel	$Åk_{60\pm2}$	84	14	2	Six hours 1332 °C then cooled to 1312 °C at 120 °C h^{-1}
DT1-1MM	1308	23.7	gl + sp + mel	$Åk_{61\pm3}$	80	16	4	Six hours 1327 °C then cooled to 1308 °C at 120 °C h^{-1}
DT1-3A	1301	45.6	gl + sp + mel	$Åk_{57-67}$			15	Five hours 1351 °C then cooled to 1301 °C at 10 °C h^{-1}
DT1-3B	1301	30.0	gl + sp + mel					Five hours 1420 °C then cooled to 1301 °C at 10 °C h^{-1}
DT1-1BB	1300	48.2	gl + sp + mel	$Åk_{58\pm6}$	70	15	15	
DT1-1Q	1281	31.9	gl + sp + mel	$Åk_{63\pm6}$	65	15	20	
DT1-1S	1258	29.9	gl + sp + mel	$Åk_{67\pm7}$			19	
DT1-1V	1246	46.7	gl + sp + mel	$Åk_{71\pm5}$	58	18	24	
DT1-1KK	1242	62.7	gl + sp + mel	$Åk_{69\pm5}$	55	20	25	
DT1-1X	1238	43.7	gl + sp + mel + an	$Åk_{80\pm5}$			29	
DT1-1R	1229	44.2	gl + sp + mel + an	$Åk_{70\pm9}$			15	
DT1-1T	1210	40.3	sp + mel + an + px	$Åk_{49\pm6}$			19	
DT1-1JJ	1200	56.6	sp + mel + an + px	$Åk_{47\pm6}$			33	
DT1-1HH	1179	58.6	sp + mel + an + px	$Åk_{47\pm5}$			39	
DT1-1EE	1149	53.2	sp + mel + an + px	$Åk_{47\pm5}$			30	Quenched in air
DT1-1J	1279	34.3	gl + sp					Five hours at 1577 °C then cooled to 1279 °C at 295 °C h^{-1}, quenched in air
DT1-1I	1230	40.0	gl + sp					Five hours at 1577 °C then cooled to 1230 °C at 245 °C h^{-1}
DT1-1L	1207	34.8	gl + sp + mel + px[d]	$Åk_{\sim60}$				Five hours at 1578 °C then cooled to 1207 °C at 245 °C h^{-1}
DT1-1K	1157	41.0	sp + mel + px[d]	$Åk_{50-67}$				Five hours at 1578 °C then cooled to 1157 °C at 263 °C h^{-1}
DT1-1M	1124	43.8	sp + mel + px + an[d]	$Åk_{55-60}$				Five hours at 1578 °C then cooled to 1124 °C at 297 °C h^{-1}, quenched in air

[a] Shown are average melilite compositions with 1σ standard deviation obtained from analysis of central parts of at least 40 individual grains.
[b] Experiments were conducted by bringing the samples directly into the furnace hot spot with temperature of interest unless noted.
[c] Bimodal size distribution of spinel grains (~10 and 50–100 μm).
[d] Dendritic melilite.

file from the top to the bottom (open circles), if taken alone, would suggest that the melilite is normally zoned outside of a small relatively åkermanite-rich core. The profile from the left to the right side of the grain (closed circles), however, is typical for a reversely zoned melilite, although the overall compositional range is narrow. The

possibility of complex zoning, including sector zoning of single crystals of melilite, makes suspect interpretations of melilite crystallization history based on a single traverse. Furthermore, as the normally zoned top-to-bottom profile shows, jumps of a few mole % Åk can occur when a different sector is crossed.

We also conducted a series of experiments in which samples of DT1 composition were first heated to $T \sim 1580$ °C for 5 h, then cooled at very high cooling rates (245–297 °C h^{-1}) to temperatures below 1315 °C and held at these temperatures for extended period of time (runs DT1-1J, -1I, -1L, -1K, and -1M in Table 3). Melilite in these experiments did not crystallize until 1207 °C, which is significantly lower than 1315 °C at which melilite was formed in isothermal experiments. This delay of more than 100 °C in melilite crystallization is probably explained by the destruction of nucleation sites for melilite while samples were heated for an extended period of time at superliquidus temperatures, as suggested by Stolper and Paque (1986). The melilite that did crystallize in our very fast cooling experiments at temperatures at or below 1207 °C (runs DT1-1L, DT1-1K, and DT1-1M) was always dendritic, again consistent with what had been found by Stolper and Paque in their experiments with cooling rates greater than 50 °C h^{-1}. The fact that the dendritic melilite texture remained even after extended heating (34–44 h) at moderately high temperatures between 1207 and 1124 °C is a reflection of low cation diffusion rates in melilite.

Anorthite and pyroxene were observed in most of our experiments with the DT1 composition at temperatures below ~1238 and ~1210 °C, respectively. Despite the large difference in the crystallization temperature of melilite in DT1 and CAIB, the crystallization temperatures of anorthite and pyroxene in DT1 are much closer to those reported by Stolper (1982) for the CAIB composition (~1260 and ~1230 °C, respectively). However, in experiments involving very fast cooling (>245 °C h^{-1}) anorthite was not observed until 1124 °C.

3.1.3. DT2

The DT2 composition is meant to represent a composition along the evaporation trajectory of DT1. All crystallization experiments using the DT2 composition were isothermal runs at temperatures above the solidus and therefore only textures similar to the one shown in Fig. 2a were found. The results of the experiments are summarized in Table 4 and Fig. 1c.

As was the case in experiments with CAIB-R and DT1 starting compositions, spinel is the first mineral to crystallize in a cooling DT2 melt. The first melilite was found at 1395 °C and it occurred as ~10–20 μm grains with $Åk_{19\pm2}$. Fig. 1c shows how the melilite becomes more abundant and more åkermanitic with falling temperature. By $T = 1299$ °C, melilite occupied ~32% of the area in the analyzed section and the central parts of the melilite grains were characterized by $Åk_{28\pm6}$. We compared quantitative maps of samples quenched in water and in air and found that the extreme outer parts of melilite grains quenched in air are significantly more åkermanitic ($Åk_{49-55}$) than the rest of the grain ($Åk_{20-28}$), which was not the case for samples quenched in water. The åkermanitic rims of the air-quenched samples are almost certainly due to melilite continuing to crystallize during the slower quenching in air compared to the much faster quenching in water. Only average compositions obtained from more than 40 analyses of central parts of the grains are shown in Fig. 1. Due to the relatively high temperatures at which the DT2 experiments were quenched, no anorthite or pyroxene was found in any of the analyzed run products.

3.2. Parameterized model for the crystallization of melilite

The experiments discussed in the preceding section provide the crystallization temperature and Åk content of melilite in three different melt compositions. Previously, Stolper (1982) had reported the crystallization temperature and Åk content for melilite crystallizing from a melt he called CAIB, which was meant to represent an average composition of the Type B CAIs. Paque and Stolper (1984) reported similar data for a composition, #98, meant to represent a typical Type B1 melilite-rich CAI. Beckett (1986) reported the crystallization temperature of melilite and its Åk content in melts with compositions close to those of fluffy Type A CAIs (FTA-1), compact Type A CAIs (CTA-1), what he considered to be average Type B1 (B1-1) and Type B2 (B2-1) CAIs. These data are combined in Fig. 5 to show the dependence of the melilite crystallization temperature on melt composition expressed in terms of the molar ratio of volatile ($MgO + SiO_2$) to refractory ($CaO + Al_2O_3$) elements, which we will abbreviate as MS/CA. The solid curve is a best fit through the experimental data that is used in later discussions of the origin of the Type B CAIs.

Fig. 5 shows that the melilite crystallization temperature is very dependent on the melt composition from which it crystallizes. As a melt becomes depleted in the more volatile components MgO and SiO_2, the crystallization temperature of melilite increases from $T \sim 1230$ °C at MS/CA = 1.2 to $T \sim 1530$ °C at MS/CA = 0.5, with an associated change in the melilite composition from $Åk_{65}$ to nearly pure gehlenite, $Åk_1$. The fact that the crystallization temperature and Åk content of melilite depend on the bulk composition of the melt from which melilite crystallizes is not a new result. However, the plot shown in Fig. 5 provides a simple means to estimate the crystallization temperature and Åk content of melilite for a broad range of CAI-like melt compositions. Fig. 5 also shows why melilite did not crystallize from the B2C melt composition of Paque and Stolper (1984) with MS/CA = 1.37. According to Fig. 5, melilite in B2C melt is expected to crystallize at temperatures much lower than 1200 °C while the experiments were conducted at 1200–1500 °C. We should caution, however, that this diagram should only be used for compositions that plot within or close to the spinel + melilite field

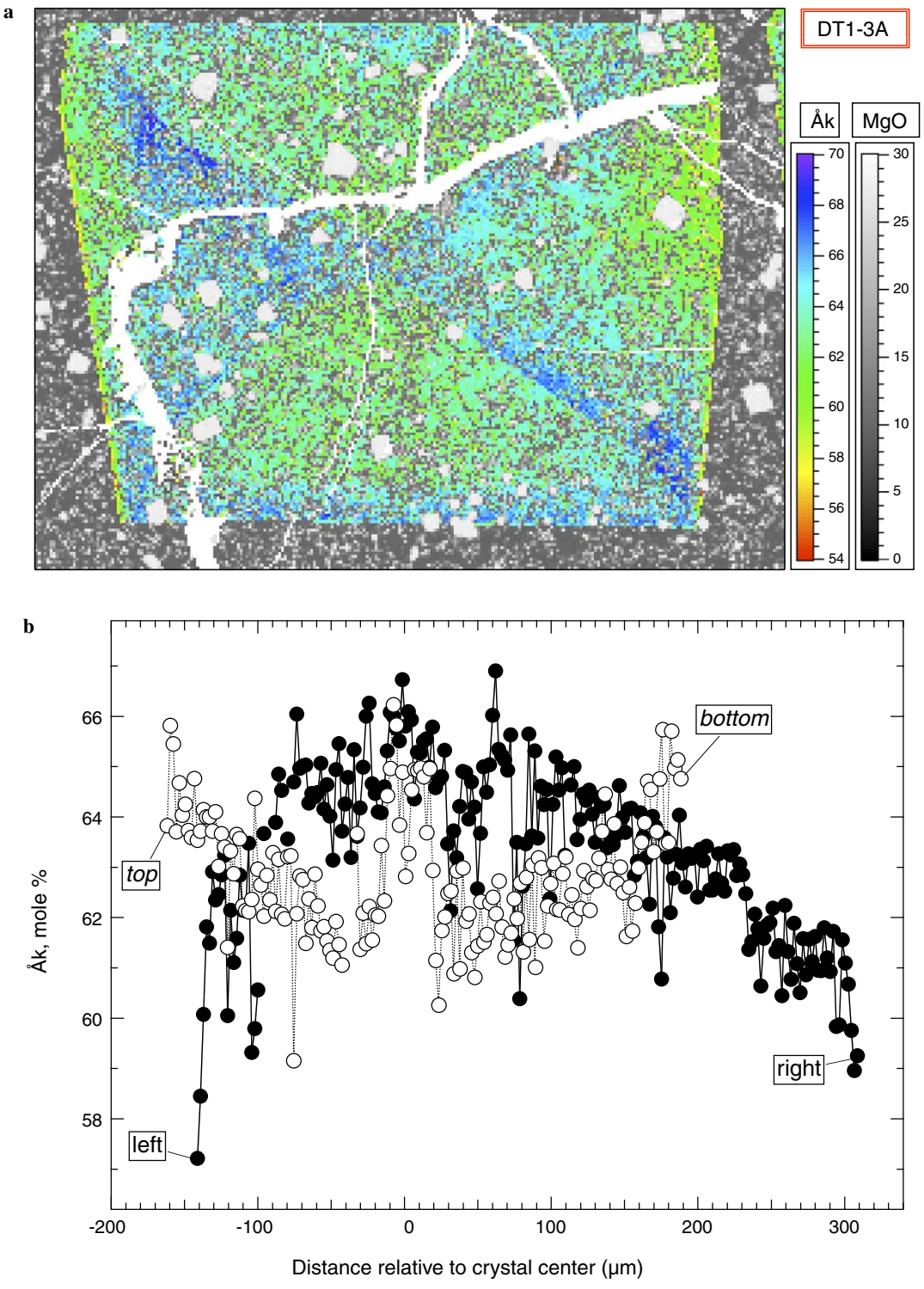

Fig. 4. Melilite zoning in a sector-zoned melilite crystal (450 μm in size) from run DT1-3A. This sample was cooled from 1351 to 1301 °C at 10 °C h^{-1} in air. (a) Melilite compositional map. (b) Åk profiles from the left to the right, and from the top to the bottom of grain passing through the center of grain shown in (a).

of Stolper's (1982) pseudo-ternary diagram. We highlight this caution by noting that Fig. 5 fails to predict the crystallization temperature and composition of melilite crystallizing from anorthite- or hibonite-rich systems, such as TCAN and ES of Paque and Stolper (1984), ETEG of Beckett (1986), and HIBs of Beckett and Stolper (1994).

The shape of the curve in Fig. 5 has important implications for how melilite can be produced in experiments or in

Table 4
Conditions and results for DT2 crystallization experiments

Run	T (°C)	Duration (h)	Phases identified	Melilite comp[a]	Vol%			Notes[b]
					gl	sp	Mel	
DT2-A	1646	1.2	gl		100			Quenched in air
DT2-H	1450	22.5	gl + sp		88	12		
DT2-E	1421	20.5	gl + sp		82	18		
DT2-B	1400	19.5	gl + sp		87	13		Quenched in air
DT2-K	1395	39.5	gl + sp + mel	$Åk_{19\pm2}$	81	15	4	
DT2-M	1389	35.5	gl + sp		88	12		Quenched in air
DT2-N	1385	35.4	gl + sp + mel	$Åk_{19\pm2}$	77	17	6	
DT2-L	1380	40.6	gl + sp + mel	$Åk_{16–49\ (18\pm2\ and\ 46\pm3)}$[c]	84	13	3	Quenched in air
DT2-G	1375	23.0	gl + sp + mel	$Åk_{21\pm3}$	75	15	10	
DT2-J	1365	32.8	gl + sp + mel	$Åk_{20\pm2}$	70	17	13	
DT2-C	1358	19.5	gl + sp + mel	$Åk_{22\pm3}$	71	15	14	
DT2-I	1345	37.0	gl + sp + mel	$Åk_{22\pm2}$	56	18	26	Quenched in air
DT2-D	1322	20.9	gl + sp + mel	$Åk_{25\pm4}$	59	12	29	Quenched in air
DT2-F	1299	64.1	gl + sp + mel	$Åk_{28\pm6}$	52	16	32	Quenched in air

[a] Shown are average melilite compositions with 1σ standard deviation obtained from analysis of central parts of at least 40 individual grains ~10–20 μm in size.
[b] Samples were heated at 1000 °C for 3 h then temperature increased at 300 °C h^{-1}. Samples were quenched in H_2O unless noted.
[c] Wide range of melilite compositions with two distinct peaks shown in parentheses.

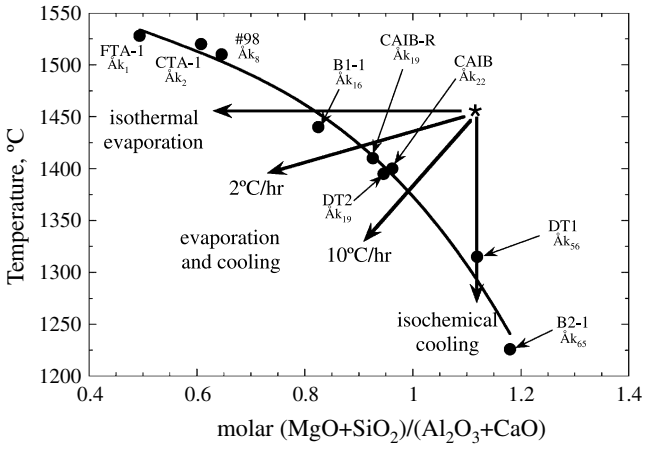

Fig. 5. Dependence of crystallization temperature of melilite on bulk composition of melt. The figure represents the summary of experimental data obtained in this study and those available in the literature. Note the significant variation in the composition of initially crystallizing melilite with melt composition. Data sources: CAIB-R, DT1, and DT2, this work; CAIB, Stolper (1982); #98, Paque and Stolper (1984); FTA-1, CTA-1, B1-1, and B2-1, Beckett (1986). The solid curve is a best fit through the experimental data ($y = 1699.7 - 606.5x + 811.5x^2 - 531.4x^3$). Also shown are possible trajectories of melilite crystallization: isochemical cooling, isothermal evaporation, and combination of cooling and evaporation.

natural settings. We illustrate this with a starting melt composition indicated in Fig. 5 by an asterisk (which could have been produced by heating the bulk composition DT1) for which melilite crystallization could result from: (1) *isochemical cooling* in sufficiently oxidizing conditions that evaporation is negligible and the bulk composition of the melt is unchanging; (2) *isothermal evaporation* under sufficiently reducing conditions that the more volatile components MgO and SiO_2 become progressively depleted relative to the more refractory CaO and Al_2O_3; (3) *combined cooling and evaporation*.

The experiments discussed in the previous section show that slow cooling of a Type B CAI-like melt under oxidizing conditions (i.e., very little or no evaporation) results in more or less randomly distributed large euhedral melilite similar to what is characteristic of natural Type B2 CAIs. These experiments also showed that as the melt becomes depleted in SiO_2 and MgO, the crystallization temperature of melilite increases by a significant amount and melilite becomes more gehlenitic. This implies that depending on degree of evaporation of volatile SiO_2 and MgO from a given molten CAI precursor, melilite of different compositions will crystallize. Another important implication is that if evaporation was sufficiently fast compared to cation diffusion within the melt, the near surface will become depleted in SiO_2 and MgO relative to the interior, and melilite would crystallize there first. This could explain how the B1 type textures are produced. If, on the other hand, evaporation is sufficiently slow (or negligible) such that diffusion can maintain the chemical homogeneity of the melt, there will be no reason for preferential crystallization of melilite near the surface and one would expect a relatively uniform distribution of melilite like that of the B2 texture. In the following sections, we will discuss evaporation experiments that test this idea as to how the B1 and B2 textures can arise.

3.3. Crystallization of melilite by evaporation of DT1 melt under reducing conditions

Composition DT1 was made to approximate the composition calculated by Grossman et al. (2002) for material condensed from a solar composition gas of total pressure 10^{-5} bar and $T = 1420$ °C. DT1 is a plausible precursor for either a Type B1 or a Type B2 CAI, but in order to match the bulk compositions of these CAI types, significant amounts of MgO (and presumably SiO_2 as well) must have

been removed by evaporation. Such evaporation of MgO and SiO_2 is to be expected during the high-temperature event that partially melted the CAI precursors and produced the typical coarse-grained igneous texture (Richter et al., 2002a). In this section, we explore the consequences of crystallizing melilite under reducing conditions such that there is significant evaporation from the partially molten sample. These experiments were conducted in two regimes: evaporation at constant temperature and evaporation during cooling at a controlled rate. Conditions and results of the experiments are presented in Table 5.

3.3.1. Isothermal evaporation

According to Fig. 5, melilite can crystallize from the DT1 melt not only by isochemical cooling at temperatures below ~1315 °C, but also by isothermal evaporation at higher temperatures. We have argued that, depending on the evaporation rate of MgO and SiO_2, either a Type B1 or a Type B2 texture could be formed: slow isothermal evaporation would result in a B2 texture, while fast evaporation would form the diagnostic melilite rim of the B1 texture (Richter et al., 2006). The bulk evaporation rate will depend on the f_{O_2} of the surrounding gas, which controls the saturation vapor pressures, and the gas flow rate, which controls the rate of removal of the saturated gases from the system. The rate of loss of volatiles from the system is effectively equivalent to the rate at which volatiles are being removed from the melt (i.e., the evaporation rate of the volatile species).

Consistent with expectations, a complete melilite rim ($Åk_{5–10}$) was found after 1 h of exposure of DT1-5L to H_2 at 1473 °C during which the sample lost about 16% of its weight. A melilite rim was also observed in experiment with DT1-4FF which lost 18% of its weight due to evaporation in H_2 at 1422 °C for 15 h. Melilite from the rim of this sample is characterized by $Åk_{5–24}$ with an average $Åk_{11\pm3}$. Eight hours of evaporation of DT1-4E in H_2 at 1351 °C resulted in only 6% weight loss and the melilite from the rim was more åkermanitic, with an average composition of $Åk_{30\pm6}$. These melilite compositions are very close to what one would expect for crystallization at $T = 1473$, 1422, and 1351 °C, based on Fig. 5. The starting composition DT1 does not crystallize melilite under oxidizing conditions until the temperature falls below about 1315 °C, thus the three experiments described above are exemplary of melilite crystallization at a fixed temperature due to the changing composition of the melt by the evaporation of its more volatile components. Detailed quantitative X-ray maps of selected areas of samples from the isothermal evaporation experiments show that most of the melilite grains are reversely zoned due to evaporation reducing the amount of magnesium and silicon in the melt while melilite was crystallizing. The Åk content of melilite in the core of the grain shown in Fig. 6 is $\sim Åk_{25}$ while the outer parts of the grain are as gehlenitic as $Åk_{13}$. Another interesting feature is that the outer parts of the charge are relatively depleted in spinel compared to central parts. The extreme edge of experimental charges exposed to H_2 is characterized by the presence of essentially pure gehlenite, non-stoichiometric spinel, hibonite, and grossite. This spinel contains less MgO (as low as 16 wt% MgO and up to 84 wt% Al_2O_3), than stoichiometric $MgAl_2O_4$ (28.3 wt% MgO, 71.7 wt% Al_2O_3) from the inner parts of the sample. Also note the more rounded shape of the spinel grains enclosed in melilite compared to the more euhedral grains in the quenched glass. These features are typical for all isothermal evaporation experiments, but they are more pronounced in the higher temperature runs where a very gehlenitic melilite forms at the evaporating surface. The relative depletion of spinel towards the surface and their round shape suggests that the original more uniformly distributed euhedral spinel began to dissolve as the melt nearest to the surface lost magnesium due to evaporation. An alternative explanation of the relative depletion of spinel near the surface is that growing melilite pushed μm-sized spinel grains out of the way. However, the lack of a spinel-enriched layer adjacent to melilite grains in our experimental charges along with the rounded shape of remaining spinel near the surface suggests that this process played a very minor role.

To further confirm that melilite rims are formed in the magnesium- and silicon-depleted outer parts of molten droplets, we conducted a set of short-duration experiments in which samples were quenched just before melilite would have started to crystallize in order that we might confirm the existence of chemical gradients due to fast evaporation. We further suppressed melilite crystallization in these experiments by melting the starting materials at 1660 °C for 8 h. Such an extended period at high temperature destroys melilite nucleation sites, with the effect of significantly lowering the temperature at which melilite first starts to crystallize. The results of the isothermal evaporation experiments in which melilite did not crystallize along with the measured MgO concentrations at the edge and in the central parts of the samples are presented in Table 6.

Concentration profiles of MgO, SiO_2, CaO, and Al_2O_3 through two experimental charges are shown in Fig. 7. Essentially flat profiles of all four oxides are observed in experiments conducted under relatively oxidizing conditions ($\log f_{O_2} \geqslant$ IW-5) as shown on the left. This clearly indicates that although the samples did lose magnesium and silicon by evaporation, diffusion within the partially molten droplet was fast enough to make the chemical gradients negligibly small. The profiles shown on the right side of Fig. 7 are typical of experiments conducted in H_2 and in H_2–CO_2 mixtures with $\log f_{O_2} \leqslant$ IW-7. The outer parts of the charges are noticeably depleted in MgO, slightly depleted in SiO_2, and noticeably enriched in the conserved Al_2O_3 components compared to the central parts. The CaO component is also conserved and therefore becomes enriched in the evaporation residue, but calcium is a sufficiently fast diffuser that its concentration gradient is highly damped. The concentration gradients at fixed tem-

Table 5
Conditions and results for DT1 evaporation experiments

Run	T (°C)		Cooling rate (°C h^{-1})	Run duration (h)	Gas comp.	Gas flow rate (cm s^{-1})	% weight loss	Phases identified	Texture	Melilite comp.[b]	Notes
	Initial	Final									
Isothermal experiments											
DT1-5L	1473			1.0	H_2	5	16	gl + sp + mel	Mel rim	$Åk_{5–10}$	
DT1-4OO	1422			2.0	H_2	5	12	gl + sp + mel	Mel rim		
DT1-4FF[a]	1422			15.2	H_2	5	18	gl + sp + mel + gros	Mel rim	$Åk_{5–24(11±3)}$	
DT1-4GG[a]	1422			22.0	H_2	5	18	gl + sp + mel + gross + hib	Mel rim	$Åk_{4–22(8±4)}$	
DT1-4I	1382			6.8	H_2	5	8	gl + sp + mel	Incomp. mel rim	$Åk_{18–24}$	
DT1-4K[a]	1382			17.8	H_2	5	10	gl + sp + mel	Mel rim	$Åk_{13–26(19±3)}$	sp $Mg_{0.52}Al_{2.32}O_4$
DT1-4P	1373			2.0	H_2	5	9	gl + sp + mel	Mel rim		
DT1-4E[a]	1351			8.3	H_2	5	6	gl + sp + mel	Mel rim	$Åk_{22–44(30±6)}$	sp $Mg_{0.84}Al_{2.11}O_4$
DT1-4G	1351			24.6	H_2	5	10	gl + sp + mel	Mel rim	$Åk_{21–29}$	
DT1-4J	1348			34.8	H_2	5	8	gl + sp + mel	Incomp. mel rim	$Åk_{22–29}$	
DT1-5O	1472			2.3	IW-8	5	24	gl + sp + mel	Mel rim	$Åk_{2–6}$	
DT1-4T[a]	1385			18.6	IW-6	1	13	gl + sp + mel	Incomp. mel rim	$Åk_{10–23}$	sp $Mg_{0.95}Al_{2.03}O_4$
Cooling experiments											
DT1-4HH[a]	1421	1265	10	15.6	H_2	5	16	gl + sp + mel + grossite?	Mel rim	$Åk_{8–34(13±3)}$	
DT1-4L[a]	1380	1249	10	13.1	H_2	5	6	gl + sp + mel	Mel rim	$Åk_{35–62(45±3,60±4)}$	sp $Mg_{0.96}Al_{2.03}O_4$
DT1-4O[a]	1380	1278	5	20.4	H_2	5	9	gl + sp + mel	Mel rim	$Åk_{19–43(23±2)}$	sp $Mg_{0.95}Al_{2.03}O_4$
DT1-4S[a]	1380	1135	5	49.0	H_2	5	10	sp + mel + px + an + hib	Mel rim	$Åk_{10–76(21±3,69±5)}$	sp $Mg_{0.86}Al_{2.09}O_4$
DT1-4Q[a]	1380	1128	5	50.4	H_2	5	9	sp + mel + px + an	Mel rim	$Åk_{20–90(25±2,58±10,87±3)}$	sp $Mg_{0.94}Al_{2.04}O_4$
DT1-4R[a]	1380	1250	2	65.0	H_2	5	10	gl + sp + mel + an + hib	Mel rim	$Åk_{9–77}$	sp $Mg_{0.86}Al_{2.09}O_4$
DT1-5M	1470	1430	5	8.6	IW-6	1	16	gl + sp + mel	Mel rim	$Åk_{5–8}$	
DT1-5C[a]	1470	1258	5	42.4	IW-6	5	22	gl + sp + mel + an	Mel rim	$Åk_{2–42(6±3,15±5)}$	
DT1-4KK	1425	1232	5	38.4	IW-6	1	12	gl + sp + mel + an	Incomp. mel rim?		
DT1-4LL	1425	1251	5	34.0	IW-6	5	12	gl + sp + mel	Incomp. mel rim?		
DT1-4W[a]	1383	1152	5	45.6	IW-6	1	13	sp + mel + px + an	Mel rim	$Åk_{27–76(46±3,70±6)}$	sp $Mg_{0.95}Al_{2.03}O_4$
DT1-4X[a]	1383	1156	2	112.0	IW-6		7	sp + mel + px + an	Incomp. mel rim?	$Åk_{28–91}$	sp $Mg_{0.95}Al_{2.03}O_4$
DT1-4BB	1377	1248	2	65.5	IW-6	1	12	gl + sp + mel	Incomp. mel rim		
DT1-4CC	1375	1237	5	28.0	IW-6	1	25	gl + sp + mel	B2-like?		
DT1-4Z	1375	1228	10	14.7	IW-6	1	2	gl + sp + mel	B2-like		
DT1-5R	1471	1182	25	11.6	IW-5	1	7		dendritic		
DT1-4JJ	1425	1229	5	39.0	IW-5	1	8	gl + sp + mel	B2-like		
DT1-5Q	1425	1228	10	19.4	IW-5	1	5	gl + sp + mel	B2-like		
DT1-4II	1425	1240	5	37.0	IW-4	1	3	gl + sp + mel	B2-like		
DT1-4EE	1379	1229	2	75.0	IW-4	1	2	gl + sp + mel	B2-like		
DT1-4AA	1384	1211	5	34.6	IW	1	0	gl + sp + mel	B2-like		
DT1-3B[a]	1421	1301	10	12.0	Air	1	0	gl + sp + mel	B2-like	$Åk_{58–69}$	
DT1-3A[a]	1351	1301	10	5.0	Air	1	0	gl + sp + mel	B2-like	$Åk_{58–68}$	

[a] Detailed X-ray maps of selected area were obtained.
[b] Range of melilite composition obtained from detailed X-ray map of selected area of the samples are shown. Numbers in parentheses show peak(s) position in Åk distribution with errors representing width at half height of peaks in Åk histograms.

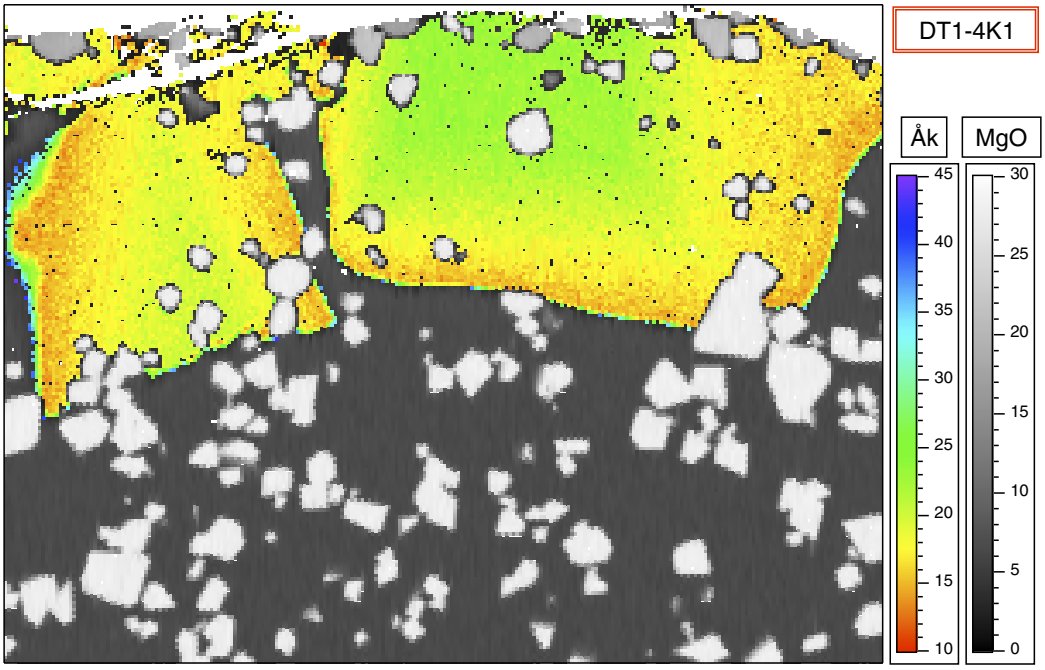

Fig. 6. Detailed Åk and MgO map of near-surface area from DT1-4K, which was evaporated isothermally in H_2 at 1382 °C. The Åk map shows reverse zoning in melilite, which is typical for melilite from the mantle produced by isothermal evaporation of partially molten droplets. The MgO map shows magnesium-depleted spinel grains (gray) within the melilite at the edge of the charge. Chemical analyses show that these spinel grains contains as low as 16 wt% MgO and up to 84 wt% Al_2O_3.

Table 6
Conditions and results for short isothermal DT1 evaporation experiments

Run	T (°C)	Run duration (h)	Gas comp.	Gas flow rate (cm s^{-1})	% weight loss	Phases identified	MgO in glass wt%
DT1-5A	1422	0.5	H_2	5	4	gl + sp	8.0–9.5
DT1-5I	1422	1.0	H_2	5	11	gl + sp	6.5–6.8
DT1-5B	1425	0.5	IW-8	5	2	gl + sp	9.5–10
DT1-5J	1425	2.1	IW-8	5	7	gl + sp	8.0–8.8
DT1-5S	1425	3.1	IW-7	5	4	gl + sp	8.0–9.0
DT1-6H	1414	3.0	IW-7	5	19	gl + sp	9.0–10.1
DT1-6P	1375	1.0	IW-7	5	1	gl + sp	10.0–10.7
DT1-6J	1375	1.0	IW-7	5	1	gl + sp	10.2–10.7
DT1-6Q	1375	2.0	IW-7	5	1	gl + sp	9.9–10.7
DT1-6R	1375	2.0	IW-7	1	1	gl + sp	9.9–10.5
DT1-6M	1375	2.5	IW-7	5	1	gl + sp	9.7–10.5
DT1-5K	1475	2.0	IW-6	5	10	gl + sp	7.0–7.9
DT1-5N	1475	2.7	IW-6	1	13	gl + sp	5.6–6.5
DT1-4NN	1425	2.0	IW-6	1	3	gl + sp	~9.5
DT1-6D	1425	3.0	IW-6	1	1	gl + sp	9.6–10.8
DT1-5E	1425	2.0	IW-6	5	4	gl + sp	~9.0
DT1-5U[a]	1377	5.1	IW-6	5	1	gl + sp	10.2–10.8
DT1-4MM	1425	0.5	IW-5	1	1	gl + sp	~10.7

[a] Detailed X-ray maps of selected area were obtained.

perature and sufficiently low f_{O_2} are independent of the run duration as shown by the runs conducted at 1375 °C and $\log f_{O_2} \sim$ IW-7 (Table 6). When the partially molten droplets were evaporated at $\log f_{O_2} \sim$ IW-6 both types of profiles shown in Fig. 7 were observed. The flat profiles are typical of the thinner samples (DT1-4NN and DT1-5E which are 1.3 and 1.2 mm thick, respectively), while thicker samples (DT1-6D and DT1-5U which are 2.9 and 3.9 mm thick, respectively) show concentration gradients. The correlation of observed concentration gradients with sample size is to be expected in that chemical diffusion will homogenize thinner samples faster than thicker ones.

3.3.2. Cooling experiments

In this section, we discuss experiments in which cooling that started immediately after a sample was introduced into hot spot of the furnace. Cooling rates from 2 to 25 °C h^{-1} were used. Some of the experimental details and results are listed in Table 5 showing that the formation of a melilite mantle strongly depends on the

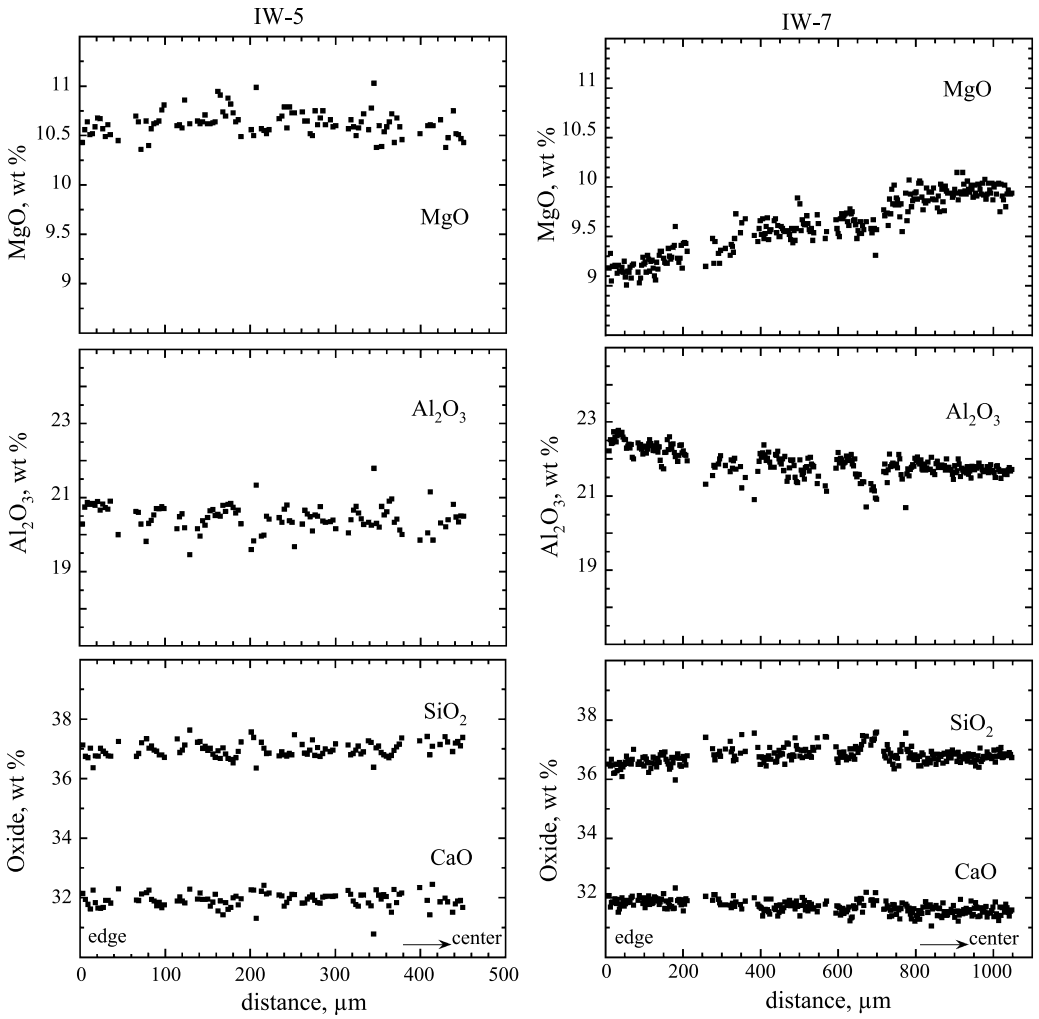

Fig. 7. Two typical oxide profiles from isothermal evaporation experiments without melilite mantle. One set of profiles was from experiments (DT1-4MM) conducted at $\log f_{O_2} \geqslant$ IW-5, the f_{O_2} at which melilite rim does not form. The profiles show essentially the same concentrations of all four oxides analyzed through the sample. The other set of profiles is from experiments (DT1-6H) conducted at $\log f_{O_2} \geqslant$ IW-7, the conditions when melilite mantle usually forms. The profiles show that the outer parts of the sample are depleted in magnesium and silicon, and enriched in aluminum relatively to the central part.

f_{O_2} of the flowing gas. Melilite mantles were formed in all experiments conducted in H_2, while only B2-like textures were produced in experiments at $\log f_{O_2} \geqslant$ IW-5. At IW-6, melilite rims were observed in two samples cooled from 1470 °C at 5 °C h^{-1} and in DT1-4W, cooled from 1383 °C at 5 °C h^{-1}. Other samples run at IW-6 and cooled from temperatures below 1425 °C resulted in either incomplete (<90% of the surface) melilite rims or B2-like textures with more or less randomly distributed melilite. The examples of experimentally produced textures with randomly distributed euhedral melilite and with well-developed melilite rim are shown in Fig. 8.

All melilite in sample DT1-4O cooled in H_2 from 1380 to 1278 °C was in a mantle, while melilite both as a mantle and in the central parts of the sample was found in DT1-4S, cooled to 1135 °C. Similarly, DT1-5M quenched at IW-6 at 1430 °C had a melilite mantle with no melilite in its central parts, while DT1-5C, quenched to a lower temperature of 1258 °C, contained melilite both in a mantle and in the central parts of the charge. These results confirm our expectation that given sufficiently reducing conditions the first melilite will crystallize at the surface forming a melilite mantle followed later by melilite crystallizing more or less randomly in the central parts of the originally molten sample.

The experiments show that, for a given cooling rate, the melilite crystallized in droplets cooled from higher maximum temperatures is more gehlenitic than that in droplets cooled from a lower maximum temperature. This is as expected because of the greater evaporation associated with the higher starting temperature. The effect of starting temperature on the åkermanite content of first melilite to crystallize is easily seen when comparing the results of experiments DT1-5M and DT1-4W listed in Table 5. The melilite composition from experiments in which samples were cooled from 1380 °C at 10, 5, and 2 °C h^{-1} in hydrogen is characterized by Åk as low as ~35, ~20, and ~15, respectively, which

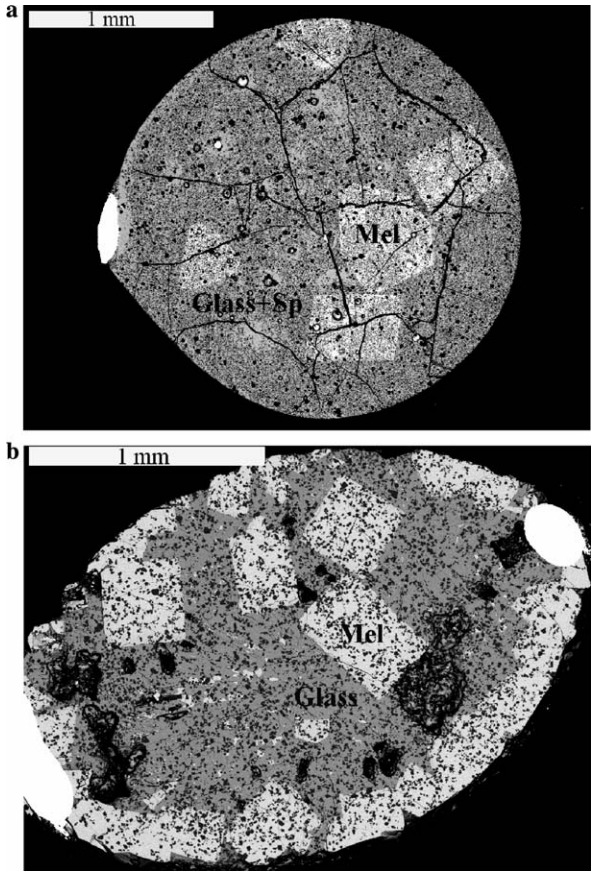

Fig. 8. Backscattered electron image of: (a) DT1-3A, crystallized by cooling DT1 melt in air with randomly distributed melilite (B2-like texture) and (b) DT1-4W, crystallized by cooling DT1 melt at IW-6 with well-developed melilite rim and randomly distributed melilite in the central parts (B1-like texture).

is also consistent with our expectations in that the faster the cooling rate, the less evaporation and thus the greater the Åk content of the first melilite to crystallize (see Fig. 5).

In experiments conducted under very reducing conditions anorthite was observed in runs quenched at temperatures as high as 1258 °C, and pyroxene only at $T = 1156$ °C. The crystallization temperature of anorthite under reducing conditions appears to be only slightly higher than under oxidizing conditions (~1238 °C, see Table 3). On the other hand, the crystallization temperatures of pyroxene from starting composition DT1 are significantly lower under reducing conditions than under oxidizing conditions (~1210 °C, Table 3). This large drop in the crystallization temperature of pyroxene under reducing conditions is most likely the result of the greater loss of magnesium from droplets exposed to extremely reducing gases.

3.4. Application of the experimental results to natural CAIs

The defining difference between Type B1 and B2 CAIs is that the B1s have a well-developed melilite mantle along with euhedral melilites in their central parts whereas the melilite in the B2s consists of relatively uniformly or randomly distributed euhedral grains. The melilite in the B1s is typically radially zoned with $\sim$Åk$_{10–20}$ near the edge of the inclusions to $\sim$Åk$_{35}$ at the core–mantle boundary and up to Åk$_{65}$ in B1 cores. Another typical feature of the Type B1 CAIs is that melilite nearest the surface is noticeably depleted in enclosed spinel. In the case of Type B2 CAIs there is no systematic distinction in the melilite composition (Åk$_{45–90}$) between the central and outer parts of the inclusion (Wark and Lovering, 1982).

Wark and Lovering (1982) have argued that many of the diagnostic properties of the Type B1 inclusions can be explained by crystallization of melilite from partially molten droplets solidifying from the outside in. They also suggested that the uniform distribution of melilite in Type B2 CAIs resulted from their being melted at lower temperatures with the effect that the melt contained abundant uniformly distributed nucleation sites. However, the reason why a given CAI-like molten droplet would crystallize from the outside inwards remains unclear. Furthermore, B1-like textures have not been produced in cooling experiments conducted under relatively oxidizing conditions regardless of maximum temperature (for an extensive set of such experiments see Stolper and Paque, 1986). Those authors were able to reproduce Type B2 textures with relatively uniformly distributed large euhedral melilite crystals in experiments cooled in air at rates up to 50 °C h^{-1} from peak temperatures only a few degrees above the crystallization temperature of melilite. We found similar results in our experiments run under oxidizing to moderately reducing conditions ($\log f_{O_2} \geqslant$ IW-4). We went on to show that a melilite mantle forms quite readily when a partially molten droplet is exposed to a very reducing gas ($\log f_{O_2} \leqslant$ IW-6). The key to forming a melilite mantle is not just that the surrounding gas must be extremely reducing but that the associated evaporation rate be sufficiently fast so that diffusion cannot maintain chemical homogeneity of the melt. In the diffusion-limited regime, the surface region will become more depleted in silicon and magnesium than the interior, which as we showed in Fig. 5 will result in melilite crystallizing first at the surface eventually producing a melilite mantle.

Our experiments represent a set of specific conditions that lead to either B1- or B2-like textures during cooling and/or evaporation of a molten droplet of CAI-like composition. These experimental results can be recast into a more generalizable form for application to natural CAIs. This is done by using the experiments to validate a general model for what determines the texture produced by crystallization of CAI-like melt. Richter et al. (2002a) have already discussed a non-dimensional parameter, the evaporation number ε_j, which provides a useful measure of the relative rates of evaporation and diffusion. The evaporation number is a ratio of the diffusive adjustment time scale τ_{diff} for a spherical droplet of radius r_0 and diffusion coefficient D_j ($\tau_{diff} = r_0^2/D_j$) to the evaporation time scale τ_{evap}, representing the time it would take to exhaust the initial amount of component j, with initial molar

density $C_{j,0}$ mol cm^{-3}, evaporating at rate $J_{j,0}(\tau_{evap} = (4/3)\pi r_0^3 C_{j,0}/4\pi r_0^2 J_{j,0} = r_0 C_{j,0}/3J_{j,0})$. The evaporation number for component j is then

$$\varepsilon_j = \frac{\tau_{diff}}{\tau_{evap}} = \frac{3J_{j,0}r_0}{C_{j,0}D_j}. \quad (4)$$

If the diffusion rate is fast compared to the evaporation rate, the diffusive adjustment time scale will be short compared to the evaporation time scale, (i.e., $\varepsilon_j < 1$) and thus diffusion will be able to maintain chemical homogeneity at all times. If, on the other hand, the diffusive adjustment time is long compared to the evaporation time scale (i.e., $\varepsilon_j > 1$), the outer parts of the droplet will become more depleted in volatile elements than the interior. Because of the compositional dependence of the melilite crystallization temperature shown in Fig. 5, melilite will then crystallize first in this near-surface region.

The key idea in its most general form is that the texture produced by crystallization from a CAI-like liquid will be similar to that of the Type B1 CAIs when $\varepsilon_{Mg} > 1$ and $\varepsilon_{Si} > 1$, while B2-like textures will form when $\varepsilon_{Mg} < 1$ and $\varepsilon_{Si} < 1$. In order to validate this using our experiments we need to calculate the relevant evaporation numbers using the evaporation rates of magnesium and silicon and the diffusion coefficients for magnesium, silicon, calcium, and aluminum in melts of Type B CAI-like compositions. The diffusion coefficients can be determined from experimental diffusion profiles such as those shown in Fig. 9. The experiments were conducted by juxtaposing melts of different CAI-like compositions (less about 10 wt% $MgAl_2O_4$ to account for a solid spinel fraction) in a piston cylinder assembly. The diffusion couples were partially annealed at a fixed temperature and a pressure of about 6 kb. The experiments were run at this pressure to ensure that any trapped gas in the starting powders would dissolve in the melt and not ruin the experiments by rising through the melt. The dissolved gas, as long as it does not contain appreciable water vapor, will have a negligible effect on the composition on the melt. Typical activation volumes for diffusion in silicate melts are sufficiently small that diffusion coefficients measured at 6 kb can be used without correction at the lower pressures relevant to molten CAIs. The MgO profile in Fig. 9 shows that magnesium diffuses considerably faster than aluminum and silicon in a Type B CAI-like melt. From similar profiles at 1475, 1500, and 1570 °C we obtained diffusion rates listed in Table 7, which allowed us to estimate the values of binary diffusion coefficients at 1400 °C in melts with Type B CAI-like compositions: $D_{Mg} = 1.0 \times 10^{-6}$ cm^2 s^{-1}, $D_{Si} = D_{Al} = 0.5 \times 10^{-6}$ cm^2 s^{-1}, $D_{Ca} = 2.0 \times 10^{-6}$ cm^2 s^{-1}. The diffusion coefficient for calcium relative to that for magnesium is based on earlier diffusion experiments reported by Richter et al. (1998). The above values for the diffusion coefficients are consistent with the results from the empirical models for multicomponent diffusion of Liang et al. (1997).

Fig. 10 shows a set of calculated oxide profiles as a function of radius for an evaporating molten droplet of Type B

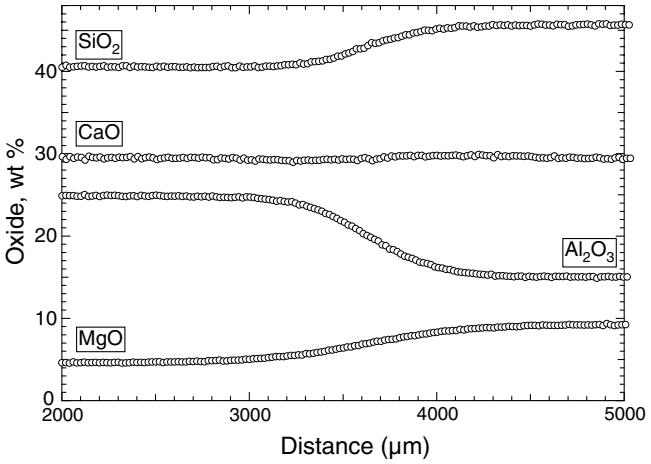

Fig. 9. Experimental diffusion profiles observed in a system slightly enriched in SiO_2 compared to average Type B composition. The experiment was conducted in piston cylinder apparatus at 1570 °C and 6 kb; run duration was 10 min. Results from this and similar experiments were used to determine diffusion rates of MgO, SiO_2, CaO and Al_2O_3 in melts of Type B composition.

CAI-like composition (with 10 wt% $MgAl_2O_4$ removed to account for crystallized spinel) using the approach described in Richter et al. (2002b) for $\varepsilon_{Mg} = 3$ and $\varepsilon_{Si} = 0.75$, and $\varepsilon_{Al} = \varepsilon_{Ca} = 0$. The figure shows that by the time the bulk loss of the MgO component is 25%, the outer portions of the model inclusion are significantly more depleted than the interior. The conserved components CaO and Al_2O_3 have both increased because of the loss of MgO and SiO_2, with the Al_2O_3 component showing the larger gradient because of its relatively slower diffusion compared to CaO. The SiO_2 shows only a weak gradient because its evaporative loss is being offset by the more rapid evaporation of the MgO, which has the effect of increasing the wt% of slower or non-evaporating components. Fig. 11 shows MgO profiles taken from the same calculation but now corresponding to 5%, 10%, 20%, and 50% of the MgO having evaporated. The interesting point is that once about 10% of the MgO has evaporated, the core to rim gradient remains relatively unchanged as MgO continues to evaporate. In Fig. 12 we show that, as expected, the major determinant of the core to rim gradient in MgO associated with evaporation is the evaporation number. This figure shows that at a low value of the evaporation number ($\leqslant 0.1$), the concentration of MgO in outer parts of the droplet is essentially the same as in central parts despite the fact that bulk sample has lost about 10% of its original MgO. At high evaporation number ($\varepsilon_{Mg} = 9.1$) the inner 2/3 of the droplet will not have yet lost any MgO while the surface concentration is almost half the initial amount. These results make clear that the evaporation number is a good measure of whether evaporation is fast or slow compared to diffusion, with the boundary between fast and slow being in the range 0.1–1.

Model profiles calculated for different evaporation numbers can be used to estimate the evaporation numbers that determined the outcome of our various evaporation experiments. By matching the measured profiles from our exper-

Table 7
Diffusion coefficients of magnesium, silicon, and aluminum as a function of temperature and SiO_2 content in melts with typical Type B CAI compositions

T (°C)	SiO_2 content					
	40 wt%			45 wt%		
	D_{Mg}	D_{Si}	D_{Al}	D_{Mg}	D_{Si}	D_{Al}
1470	3.6×10^{-6}	1.1×10^{-6}	1.6×10^{-6}	2.5×10^{-6}	8.0×10^{-7}	1.35×10^{-6}
1500	4.55×10^{-6}	2.67×10^{-6}	2.4×10^{-6}	4.0×10^{-6}	1.5×10^{-6}	1.2×10^{-6}
1570	1.15×10^{-5}	2.67×10^{-6}	4.5×10^{-6}	4.9×10^{-6}	1.5×10^{-6}	1.5×10^{-6}
1400[a]	1.0×10^{-6}	1.0×10^{-6}				

[a] Estimated values from Richter et al. (2002a).

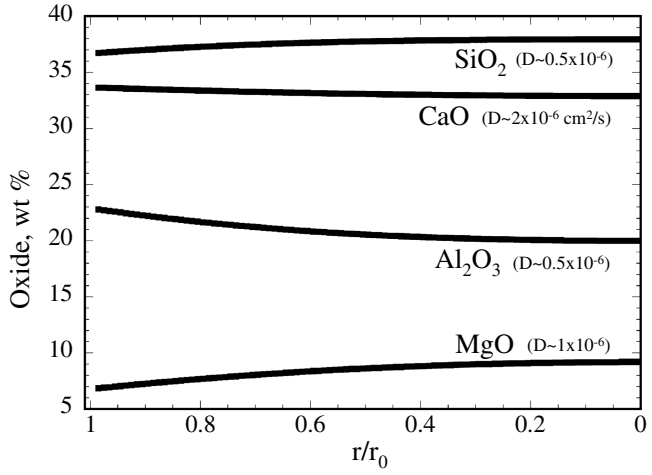

Fig. 10. Calculated profiles of MgO, SiO_2, CaO, and Al_2O_3 at 1400 °C in 3 mm diameter droplet of CAI-like composition after loss of 25% of MgO ($\varepsilon_{Mg}=3$, $\varepsilon_{Si}=0.75$, $\varepsilon_{Al}=\varepsilon_{Ca}=0$).

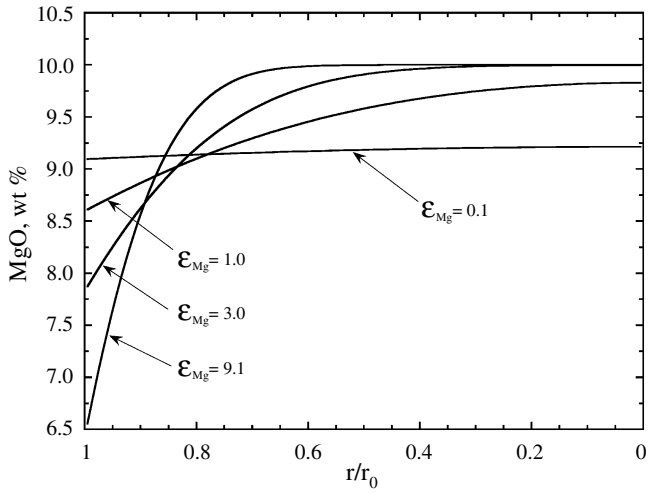

Fig. 12. Calculated MgO profiles in 3 mm diameter droplet of CAI-like composition as a function of evaporation numbers ($T=1400$ °C).

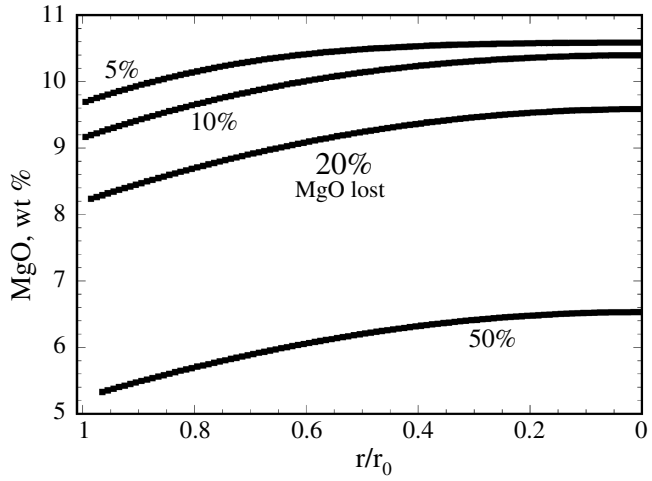

Fig. 11. Calculated MgO profiles in 3 mm diameter droplet of CAI-like composition after loss of 5%, 10%, 20%, and 50% of the MgO at 1400 °C ($\varepsilon_{Mg}=3$).

iments conducted at different f_{O_2} values with calculated ones using different magnesium evaporation numbers will allow us to estimate minimum ε_{Mg} at which Type B1-like textures are formed. Fig. 13 illustrates how we determine the evaporation numbers that can explain a set of experimentally measured profiles in DT1-6Q, which was evaporated at 1385 °C and $\log f_{O_2}\sim$ IW-7. Measured and calculated profiles match very nicely for $\varepsilon_{Mg}=0.9$. When the same conditions that produced the profiles shown in Fig. 13 were maintained for longer times in very similar experiments, melilite was found to have crystallized from the surface inwards to produce a melilite mantle. From this we conclude that the formation of melilite rims in our experiments will arise once the evaporation number for Mg is equal or greater to about one. In a similar way we found that experimental profiles conducted at $\log f_{O_2}<$ IW-6 that were matched with values of ε_{Mg} less than about 0.3 only produced B2-like texture. Experiments with ε_{Mg} between ~0.3 and ~0.9 usually produced incomplete melilite rims that could be regarded as transitional between the typical B1 and B2 textures. Eq. (4) shows that for a system with given size and starting composition melt droplet, the evaporation factor will depend on the evaporation, which for evaporation into a low pressure of surrounding gas can be described by the Hertz–Knudsen equation (Eq. (3)). In case of magnesium and silicon, when the dominant gas species are Mg and SiO, Eq. (3) simplifies to:

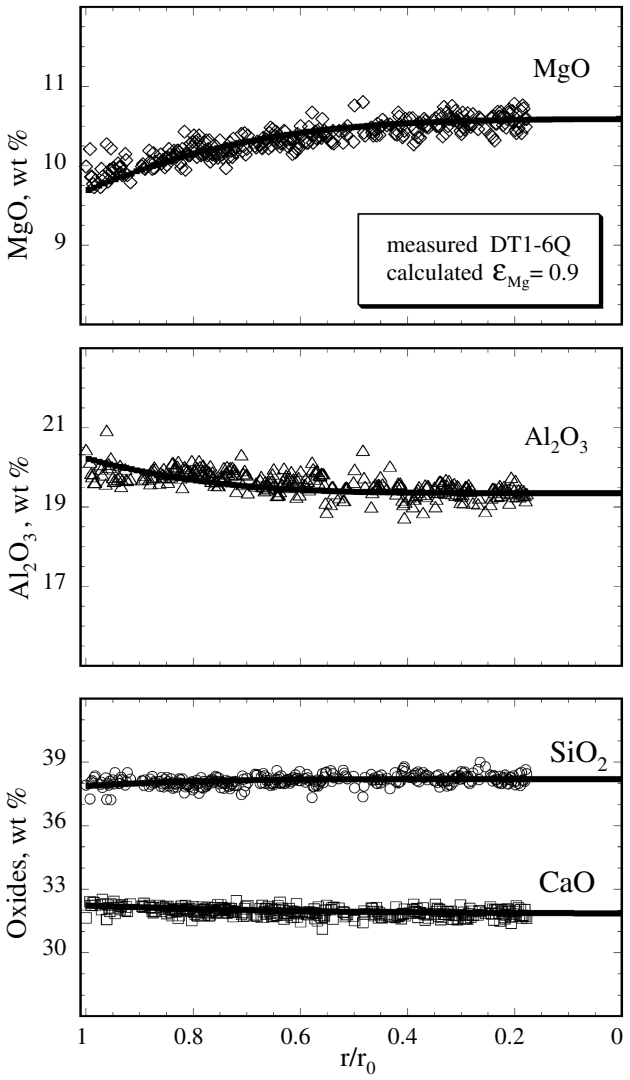

Fig. 13. Calculated and measured profiles from the evaporation experiment DT1-6Q conducted at 1385 °C and $\log f_{O_2} \sim$ IW-7. Measured and calculated profiles match nicely for $\varepsilon_{Mg} = 0.9$.

$$J_{Mg} = \frac{\gamma_{Mg} P_{Mg,sat}}{\sqrt{2\pi m_{Mg} R_0 T}} \quad \text{and} \quad J_{Si} = \frac{\gamma_{Si} P_{SiO,sat}}{\sqrt{2\pi m_{SiO} R_0 T}}. \qquad (5)$$

Richter et al. (2002a) showed that in a hydrogen-dominated regime ($10^{-7} < P_{H_2}$ (bar) $< 10^{-3}$) the evaporation rate of magnesium, J_{Mg}, will increase as $\sqrt{P_{H_2}}$ because of the dependence of the saturation vapor pressure on P_{H_2} (i.e., $P_{Mg,sat} \propto \sqrt{P_{H_2}}$). This, together with the fact that the activation energies for diffusion in a melt of CAI-like composition and for evaporation are very similar (Richter et al., 2002a), means that their ratio in Eq. (4) will be relatively insensitive to temperature, the main determinant of the evaporation number will be hydrogen pressure with $\varepsilon_{Mg} \propto \sqrt{P_{H_2}}$. This implies that a constraint on the ε_{Mg} required to make melilite mantles translates into a constraint on the pressure in a solar nebular gas. Richter et al. (2006) used this approach to argue that a cm-sized Type B1 CAIs could form by evaporation of a partially molten precursor

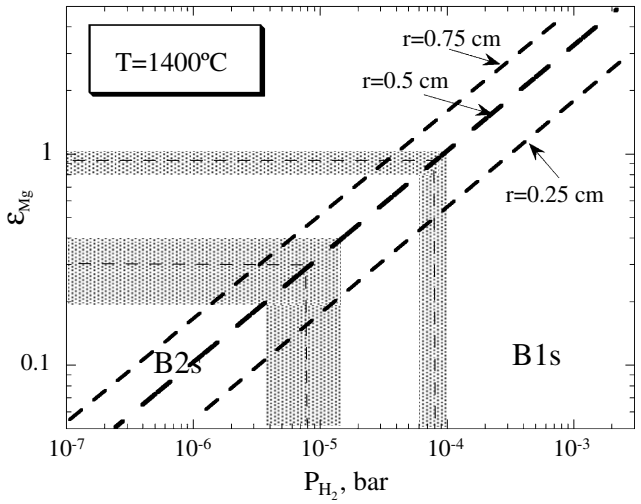

Fig. 14. Estimated pressures required for formation of Type B1 and Type B2 CAIs in the solar nebula. The formation of melilite mantle (as in B1s) in experiments requires the evaporation number for Mg to be equal or greater than about one, which for a cm-sized objects transforms into $P_{H_2} \geqslant 10^{-4}$ bar. Randomly distributed melilite grains in our experiments (as in B2s) were observed when evaporation number for Mg was lower than 0.3, which corresponds to $P_{H_2} \leqslant 10^{-5}$ bar in the solar nebula.

in regions of the solar nebula with $P_{H_2} \geqslant 10^{-4}$ bar. Type B2 CAIs could form by slower evaporation of the same precursors requiring $P_{H_2} \leqslant 10^{-5}$ bar. In Fig. 14, we translate the constraints on ε_{Mg} that we developed using our experiments into bounds on the pressure of a solar composition gas surrounding molten Type B CAI precursors of various sizes. Our estimated pressures for the transition between conditions that would make a Type B1 or a B2 texture fall well within the range of pressures predicted by the astrophysical models (e.g., Boss, 1998; Cassen, 2001) for those parts of the solar nebula where silicates are believed to have condensed.

4. Summary and conclusions

We have argued that the formation of the diagnostic melilite mantles of the Type B1 CAIs and their absence in Type B2 CAIs is due to the rates of evaporation of magnesium and silicon being fast or slow compared to their diffusion rate in the melt. If diffusion rates are sufficiently fast compared to the evaporation rate, droplets would remain chemically homogeneous and melilite would nucleate randomly throughout the melt, producing a Type B2-like texture. If, however, the diffusion rates are too slow to maintain chemical homogeneity during evaporation, the outer parts of molten droplets would become depleted in magnesium and silicon compared to the interior and melilite would crystallize there first (Fig. 5) producing a melilite mantle. To further test this idea we conducted a set of experiments in flowing gas of different f_{O_2} as a way of controlling the evaporation rate. The results of these experiments showed that for fast evaporation under very reducing conditions ($\log f_{O_2} <$ IW-6) melilite crystallized first at the surface of the molten droplets forming a melilite

mantle followed by additional more random crystallization in the inner parts of the sample at lower temperatures. We showed that such melilite mantles are produced not only during cooling of a melt, but can also be produced isothermally given sufficient evaporation and its effect on raising the crystallization temperature of melilite.

Our proposition that the melilite mantles in our experiments formed in the outer parts of molten droplets that were locally depleted in magnesium and silicon by evaporation was tested by a series of evaporation experiments at different f_{O_2}s to determine the existence of concentration gradients prior to melilite crystallization. Experimental charges run in relatively oxidizing gases such that there would have been little or no evaporation ($\log f_{O_2} \geqslant$ IW-4) have no core to rim chemical gradients (see Fig. 7) resulting in conditions such that melilite would crystallize more or less randomly throughout to produce a Type B2-like texture. On the other hand, the concentration profiles in those experiments (see Figs. 7 and 13) conducted in very reducing conditions showed that the outer parts of the experimental charges became significantly depleted in magnesium and enriched in aluminum. By comparing the shapes of the measured experimental profiles with model calculations we determined that evaporation numbers ε_{Mg} (the ratio of the diffusion time scale to the evaporation time scale) need to be greater than 0.9 in order that the surface region becomes sufficiently depleted in magnesium for a melilite mantle to form. When $\varepsilon_{Mg} \leqslant 0.3$ no measurable concentration gradient was observed and melilite would be expected to crystallize more or less randomly throughout as the temperature was further reduced.

Because temperature has the similar effect on both the evaporation rate and the diffusion rate (Richter et al., 2002a,b), the major determinant of the evaporation number of a molten Type B CAI-like droplet in the solar nebula is the surrounding pressure which affects the evaporation rate, but not the diffusion rate. The upshot of this is that a constraint on the evaporation number can be translated into a constraint on the surrounding pressure of a solar composition gas. By this approach we estimated that Type B1 CAIs could form by the evaporation of their precursor materials in parts of the solar nebula with $P_{H_2} > 10^{-4}$ bar, and Type B2 CAIs by the evaporation of the same or similar precursors at $P_{H_2} < 10^{-5}$ bar. These pressure conditions are within the range of pressures that have been suggested by astrophysical model calculations of conditions in the early solar nebula. One should keep in mind, however, that the pressures we have associated with the formation of the Type B1 and Type B2 CAIs may well be transients during the short-lived heating event that melted and gave the Type B CAIs their obvious igneous texture.

Acknowledgments

This work was supported by the National Aeronautics and Space Administration through Grants NAG5-13027 (F.M.R.) and NAG5-12997 (A.M.D.). We thank Yan Liang for conducting the CMAS diffusion runs, and R. Hewins and H. Connolly for reviewing the paper.

Associate editor: Alexander N. Krot

References

Allègre, C.J., Manhes, G., Göpel, C., 1995. The age of the Earth. *Geochim. Cosmochim. Acta* **59**, 1445–1456.

Amelin, Y., Krot, A.N., Hutcheon, I.D., Ulyanov, A.A., 2002. Lead isotopic ages of chondrules and calcium–aluminum-rich inclusions. *Science* **297**, 1678–1683.

Beckett, J.R., 1986. *The origin of calcium-, aluminum-rich inclusions from carbonaceous chondrites: an experimental study*. Ph.D. thesis, University of Chicago.

Beckett, J.R., Mendybaev, R.A., 1997. The measurement of oxygen fugacities in flowing gas mixtures at temperatures below 1200 °C. *Geochim. Cosmochim. Acta* **61**, 4331–4336.

Beckett, J.R., Stolper, E., 1994. The stability of hibonite, melilite and other aluminous phases in silicate melts: implications for the origin of hibonite-bearing inclusions from carbonaceous chondrites. *Meteoritics* **29**, 41–65.

Boss, A.P., 1998. Temperatures in protoplanetary disks. *Annu. Rev. Earth Planet. Sci.* **26**, 53–80.

Cassen, P., 2001. Nebular thermal evolution and the properties of primitive planetary materials. *Meteorit. Planet. Sci.* **36**, 671–700.

Clayton, R.N., Mayeda, T.K., Epstein, S., 1978. Isotopic fractionation of silicon in Allende inclusions. In: *Proceedings of the 9th Lunar Planetary Science Conference*, pp. 1267–1278.

Davis, A.M., Mendybaev, R.A., Richter, F.M., 2003. Evaporation of CMAS-liquids under reducing conditions: constraints on the formation of Type B1 CAIs. In: *Evolution of Solar System Materials: A New Perspective from Antarctic Meteorites*. National Institute for Polar Research, Tokyo, pp. 17–18.

Dowty, E., 1976. Crystal-structure and crystal-growth: II. Sector zoning in minerals. *Am. Mineral.* **61**, 460–469.

Grossman, L., 1972. Condensation in the primitive solar nebula. *Geochim. Cosmochim. Acta* **36**, 597–619.

Grossman, L., 1975. Petrography and mineral chemistry of Ca-rich inclusions in the Allende meteorite. *Geochim. Cosmochim. Acta* **39**, 438–451.

Grossman, L., Ebel, D.S., Simon, S.B., Davis, A.M., Richter, F.M., Parsad, N.M., 2000. Major element chemical and isotopic compositions of refractory inclusions in C3 chondrites: the separate roles of condensation and evaporation. *Geochim. Cosmochim. Acta* **64**, 2879–2894.

Grossman, L., Ebel, D.S., Simon, S.B., 2002. Formation of refractory inclusions by evaporation of condensate precursors. *Geochim. Cosmochim. Acta* **66**, 145–161.

Liang, Y., Richter, F.M., Chamberlin, L., 1997. Diffusion in silicate melts: III. Empirical models for multicomponent diffusion. *Geochim. Cosmochim. Acta.* **61**, 5295–5312.

Lugmair, G.W., Shukolyukov, A., 2001. Early solar system events and timescales. *Meteorit. Planet. Sci.* **36**, 1017–1026.

MacPherson, G.J., 2003. Calcium–aluminum-rich inclusions in chondritic meteorites. In: Davis, A.M. (Ed.), *Meteorites, Planets, and Comets*. In: Holland, H.D., Turekian, K.K. (Eds.), *Treatise on Geochemistry*, vol. 1. Elsevier-Pergamon, Oxford, pp. 201–246.

MacPherson, G.J., Wark, D.A., Armstrong, J.T., 1988. Primitive material surviving in chondrites: refractory inclusions. In: Kerridge, J.F., Matthews, M.S. (Eds.), *Meteorites and the Early Solar System*. The University of Arizona Press, Tucson, pp. 746–807.

Meeker, G.P., 1995. Constraints on formation processes of two coarse-grained calcium–aluminum-rich inclusions: a study of mantles, islands and cores. *Meteoritics* **30**, 71–84.

Mendybaev, R.A., Beckett, J.R., Stolper, E., Grossman, L., 1998. Measurement of oxygen fugacities under reducing conditions: non-Nernstian behavior of Y_2O_3-doped zirconia oxygen sensors. *Geochim. Cosmochim. Acta* **62**, 3131–3139.

Mendybaev, R.A., Beckett, J.R., Grossman, L., Stolper, E., Cooper, R.A., Bradley, J.P., 2002. Volatilization kinetics of silicon carbide in reducing gases: an experimental study with applications to the survival of presolar grains in the solar nebula. *Geochim. Cosmochim. Acta* **66**, 661–682.

Mendybaev, R.A., Davis, A.M., Richter, F.M., 2003a. Evaporation of CMAS-liquids under reducing conditions: constraints on the formation of the melilite mantle of Type B1 CAIs. *Meteorit. Planet. Sci.* **38**, A100 (abstr.).

Mendybaev, R.A., Richter, F.M., Davis, A.M., 2003b. Formation of the melilite mantle of the Type B1 CAIs: experimental simulations. *Lunar Planet. Sci.* **XXXIV**, #2062 (abstr.).

Molini-Velsko, C., Mayeda, T.K., Clayton, R.N., 1986. Isotopic composition of silicon in meteorites. *Geochim. Cosmochim. Acta* **50**, 2719–2726.

Paque, J.M., Stolper, E., 1984. Crystallization experiments on a range of Ca–Al-rich inclusion compositions. *Lunar Planet. Sci.* **XV**, 631–632 (abstr.).

Richter, F.M., Liang, Y., Minarik, W.G., 1998. Multicomponent diffusion and convection in moltem $MgO–Al_2O_3–SiO_2$. *Geochim. Cosmochim. Acta* **62**, 1985–1991.

Richter, F.M., Davis, A.M., Ebel, D.S., Hashimoto, A., 2002a. Elemental and isotopic fractionation of Type B calcium-, aluminum-rich inclusions: experiments, theoretical considerations, and constraints on their thermal evolution. *Geochim. Cosmochim. Acta* **66**, 521–540.

Richter, F.M., Davis, A.M., Mendybaev, R.A., 2002b. How the Type B1 CAIs got their melilite mantle. *Lunar Planet. Sci.* **XXXIII**, #1901 (abstr.).

Richter, F.M., Mendybaev, R.A., Davis, A.M., 2006. Conditions in the protoplanetary disk as seen by the Type B CAIs. *Meteorit. Planet. Sci.* **41**, 83–93.

Simon, S.B., Grossman, L., 2003. Insights into the formation of type B2 refractory inclusions. *Lunar Planet. Sci.* **XXXIV**, #1796 (abstr.).

Skulski, T., Minarik, W., Watson, E.B., 1994. High-pressure experimental trace-element partitioning between clinopyroxene and basaltic melts. *Chem. Geol.* **117**, 127–147.

Steele, I.M., Peters, M.T., Shaffer, E.E., Burnett, D.S., 1997. Minor element partitioning and sector zoning in synthetic and meteoritic anorthite. *Geochim. Cosmochim. Acta* **61**, 415–423.

Stolper, E., 1982. Crystallization sequences of Ca–Al-rich inclusions from Allende: an experimental study. *Geochim. Cosmochim. Acta* **46**, 2159–2180.

Stolper, E., Paque, J.M., 1986. Crystallization sequences of Ca–Al-rich inclusions from Allende: the effects of cooling rate and maximum temperature. *Geochim. Cosmochim. Acta* **50**, 1785–1806.

Wark, D.A., Lovering, J.F., 1982. The nature and origin of type B1 and B2 Ca–Al-rich inclusions in the Allende meteorite. *Geochim. Cosmochim. Acta* **46**, 2581–2594.

Wasserburg, G.J., Lee, T., Papanastassiou, D.A., 1977. Correlated O and Mg isotopic anomalies in Allende inclusions. II—Magnesium. *Geophys. Res. Lett.* **4**, 299–302.